École des Ponts ParisTech

2016-2017

PFE report

Operational coupling in coastal oceanography

Joao Guilherme CALDAS STEINSTRAESSER

IMI - Ingénierie Mathématique et Informatique

Advisor: M. Antoine ROUSSEAU

MERIC - Marine Energy Research & Innovation Center

Avenida Apoquindo 2827, piso 12 - Las Condes – Santiago, Chile

July 2017 - January 2018

Contents

1 Introduction

The work developed in this project consists on the coupling of two different wave propagation models: a spectral one, designed for describing wave propagation in large scales, and a nonlinear dispersive one, which describes nearshore small scale waves. The models used here are respectively WAVEWATCH III® and BOSZ.

1.1 Context

This project took place in the Marine Energy Research & Innovation Center (MERIC), in Santiago (Chile), and was directed by Antoine ROUSSEAU (Inria Sophia-Antipolis, LEMON team), also in collaboration with France Énergies Marines.

MERIC is an excellence center dedicated to the scientific research, technological development and innovation linked to the marine renewable energy, aiming to establish a Chilean and international reference on this subject. Created by the naval French enterprise Naval Group (formerly DCNS), MERIC is funded by CORFO (the governmental Chilean organization for promotion of economic development) and the Chilean Energy Ministry, and conducts its activities in partnership with Inria Chile, universities (Pontificia Universidad Catolica de Chile and Universidad Austral de Chile), energy enterprises (Enel Green Power Chile and Chilectra) and institutions for innovation (Fundacion Chile).

The marine energy has a very huge importance in the context of renewable energy and sustainable development, pushing up the researches on this very recent subject for developing the related technologies and reducing their costs.

The Chilean natural characteristics make this study even more relevant: with more than 6000 kilometers of coast, the tidal and waves movements originate a huge energetic potential. Furthermore, the extreme natural phenomena due to the intense seismic activity in the region demand specific studies for a safe and durable production of marine energy.

In this context, MERIC conducts a very multidisciplinary research, covering the many aspects concerning the marine energy: the study of potential areas for its production in the Chilean coast (resource assessment and site characterization); impacts on the materials in selected Chilean environments (marine corrosion and *biofouling*); environmental and social impacts (ecosystem assessment, study on marine mammals, social perception of the marine energy); technology development and its adaptation to the Chilean environment; the study of the Chilean legislation concerning the subject; development of a validation test bench; and the mathematical modeling for marine energy. The work developed in this project is part of this last research line.

1.2 Objectives

In the context of mathematical modeling and numerical simulation for the marine energy, we aim in this project to construct a coupled numerical model that would be able to model wave propagation in domains covering both offshore regions, where spectral models are used, and nearshore regions, better described by nonlinear dispersive (Boussinesq-type) models.

There are several differences between these two types kinds of models. The most important is the nature of the description of the wave propagation, which reflects in their governing equations. While spectral models work with a statistical and phase-averaged description of the waves, solving the evolution of its energy spectrum, Boussinesq-type models are phase-resolving and solve nonlinear dispersive shallow water equations for physical variables (surface elevation and velocity) in the time domain. Furthermore, the time and spatial scales for the models are very different: they are much larger in the case of spectral models, which explains its use for modeling off-shore propagation within relatively large time windows; on the other hand, important small scale phenomena in nearshore areas can be better captured by Boussinesq models, in which the time step is limited by the CFL condition.

Taking into account the collaborations involved in this project, the spectral model used here is WAVEWATCH III®, developed at NOAA/NCEP[1], and to which we refer in this project as WW3. The work in this internship included an one-week formation in this software, in the European University Institute for Marine Research (IUEM), in Brest (France).

Concerning the time-domain model, many options were considered, all of them linked with the context in which this project is inserted. The BOSZ model, developed by [17], was used, and all the work presented in the report considers this model. Nevertheless, for the sequel of the project, this choice remains open, and the model can be changed depending on our needs and some characteristics of each model, notably the types of boundary conditions that can be used. Anyway, the coupling was developed in such way that replacing one model by another could be relatively straightforward.

The work developed here covers both numerical and mathematical aspects. Concerning the implementation, the main objective is to make both softwares work together and manage their synchronization, their execution times and the exchange of informations. It is made via the coupling software OpenPalm (which we refer here as PALM), developed by CERFACS [2]. Several difficulties were imposed when integrating both models into PALM, including compilation and compatibility issues.

From the mathematical and modeling point of view, the project consists mainly in working on the boundary conditions of each model. Firstly, we have to manage the simultaneous work with spectral and timeseries data. In a second moment, we seek to study transparent boundary conditions (TBCs) for the models and develop domain decomposition approaches, for example the Schwarz methods, to model the interface boundary conditions and improve the exchange of informations (and thus the results given by the coupled model). Such study includes both the derivation of (approximate) TBCs and the anaylisis of the well-posedness of the problem when they are used as boundary conditions.

This mathematical study has been the main subject developed in the "Stage Ingénieur" for ENPC in 2016, also in MERIC and directed by Antoine ROUSSEAU, but in the context of another Boussinesq model (the KdV equation)[3]. Thus, the work proposed here can be seen as a natural continuation of the experience of this former internship.

[1] http://polar.ncep.noaa.gov/waves/wavewatch/

[2] http://www.cerfacs.fr/globc/PALM_WEB/

[3] A paper was written during that internship and is currently under revision; its notice can be consulted in HAL platform : https://hal.inria.fr/hal-01617692

The coupling developed here is designed for one-dimensional simulation. A testcase, simulating the flow over a sandbank near the Atlantic French coast, is presented to test the proposed coupling scheme. As we do not dispose of real output data (we use as reference solution he results given by a 2D simulation using WW3), we cannot validate the results, but we are able to compare the results given by the coupled model and by simulations using each individual model in the entire domain.

This report is organized as follows : in Section 2 we make an overview of each one of the models, briefly describing their governing equations, numerical aspects and input and output data. In Section 3 we present the proposed coupling scheme, describing how the models are incorporated into PALM and how we exchange the information between them. Numerical simulations on a 1D testcase, for testing the coupling and comparing its results with the ones given by the models individually, are presented in Section 4. In Section 5, we study and propose approximate TBCs for the (linearized) equations solved by BOSZ, as an initial step for improving the data transmission through the interfaces in the coupled model. Finally, in Section 6, we study the well-posedness of the problem using the proposed TBCs. Aditionnal details on the work developed are presented in three appendices.

2 The models

We present in this section the wave propagation models coupled in this project. Besides their governing equations and main physical and implementation properties, we focus on their characteristics that are specially relevant for the coupling scheme, namely their input and output data and some aspects concerning their execution.

2.1 WAVEWATCH III®

2.1.1 Governing equations

WW3, developed at NOAA/NCEP (National Oceanic and Atmospheric Administration / National Centers for Environmental Prediction), models wave propagation considering a random-phase/amplitude model. The following brief description of ocean waves under this model is based on [16] and [10, chapters 3,4].

In any specific location, the sea surface elevation is described as function of time as the sum of harmonic components with amplitude $a_{i,j}$, wavenumber k_i, relative frequency σ_i and phase $\alpha_{i,j}$:

$$\eta(t) = \sum_i \sum_j a_{i,j} \cos\left(\sigma_i t - k_i x \cos\theta_j - k_i y \sin\theta_j + \alpha_{i,j}\right) \tag{1}$$

In this model, for each frequency σ_i and each direction θ_j, both the phase $\alpha_{i,j}$ and the amplitude $a_{i,j}$ are random variables, being fully characterized by their probability density function, respectively a uniform distribution and a Rayleigh distribution with expected value $\mu_{i,j} = E\{a_{i,j}\}$:

$$p(\alpha_{i,j}) = \frac{1}{2\pi}, \qquad 0 < \alpha_{i,j} < 2\pi \tag{2}$$

$$p(a_{i,j}) = \frac{\pi}{2} \frac{a_{i,j}}{\mu_{i,j}^2} \exp\left(-\frac{\pi a_{i,j}^2}{4\mu_{i,j}^2}\right), \qquad a_{i,j} > 0 \tag{3}$$

Figure 1 illustrates the construction of a discrete frequency spectrum under the hypotheses of this model:

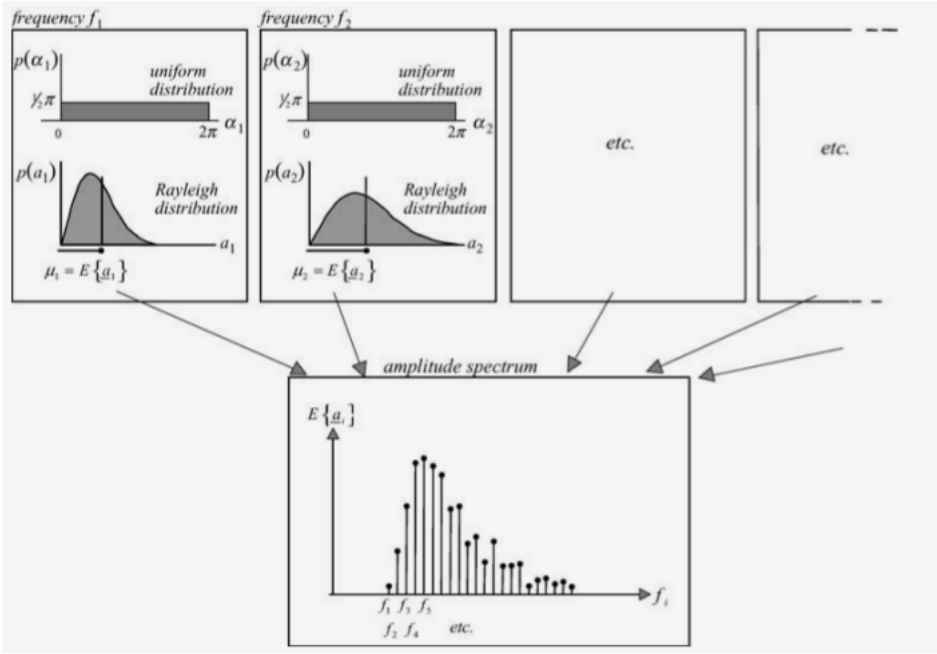

Figure 1: Construction of a discrete frequency spectrum in the random-phase/amplitude model. Figure from [10, figure 3.6]

Considering the idea presented in Figure 1 and passing it to the limit, the frequency-direction spectrum is defined from the expected value of the random variable a:

$$E\left(f_r,\theta\right)=\lim_{\Delta f_r\to 0}\lim_{\Delta\theta\to 0}\frac{1}{\Delta f_r\Delta\theta}E\left\{\frac{1}{2}a^2\right\}$$

where $f_r = \sigma/(2\pi)$ is the relative frequency, defined for a referential moving with the mean current (with velocity $\mathbf{U}$).

The integration of $E(f_r,\theta)$ over all the directions gives the frequency spectrum

$$E(f_r)=\int_0^{2\pi}E(f_r,\theta)d\theta$$

Even if the WW3 output gives the more traditional frequency-direction spectrum $E(f_r,\theta)$, its equations are written for the wavenumber-direction spectrum $E(k,\theta)$, which can be obtained by

$$E(k,\theta)=\frac{c_g}{2\pi}E(f_r,\theta)$$

where $c_g = \partial\sigma/\partial k$ is the group velocity.

Another important definition is the action density spectrum

$$N\left(k,\theta\right)=E\left(k,\theta\right)/\sigma$$

where the relative angular frequency $\sigma = 2\pi f_r$ is related to the mean water depth d by the dispersion relation

$$\sigma^2 = gk \tanh kd \tag{4}$$

and to the absolute frequency $\omega = 2\pi f_a$ by

$$\omega = \sigma + \mathbf{k} \cdot \mathbf{U}$$

The action density spectrum N is conserved during propagation in the presence of ambient current. For this reason, WW3 solves the action balance equation, which, in Cartesian coordinates, models the evolution of $N = N(k, \theta; \mathbf{x}, t)$:

$$\begin{aligned} \frac{\partial N}{\partial t} + \nabla_x \cdot \dot{\mathbf{x}} N + \frac{\partial}{\partial k}\dot{k}N + \frac{\partial}{\partial \theta}\dot{\theta}N &= \frac{S}{\sigma}, \\ \dot{\mathbf{x}} &= \mathbf{c}_g + \mathbf{U}, \\ \dot{k} &= -\frac{\partial \sigma}{\partial d}\frac{\partial d}{\partial s} - \mathbf{k} \cdot \frac{\partial \mathbf{U}}{\partial s}, \\ \dot{\theta} &= -\frac{1}{k}\left[\frac{\partial \sigma}{\partial d}\frac{\partial d}{\partial m} + \mathbf{k} \cdot \frac{\partial \mathbf{U}}{\partial m}\right] \end{aligned} \tag{5}$$

with the coordinates s and m respectively parallel and perpendicular to the direction θ, and $\mathbf{c}_g = (c_g \sin\theta, c_g \cos\theta)$.

In equation (5), S represents the source term for wave energy. Many physical processes are parametrized and included in this term, for example wave-bottom, wind-wave, wave-wave and wave-ice interactions. As the wave propagation is considered to be linear, nonlinear effects are also included in the source term S.

Moreover, in equation (5), it is implicitly assumed that the wave field, the water depth and the current vary on time and space scales that are much larger than the variation scales of a single wave.

2.1.2 The significant wave height

Among the many any statistical informations can be defined in the study of waves, one of the most important is the significant wave height ($H_{1/3}$), which is defined as the mean value of the highest one-third of wave heights in an observation. As pointed by [10], experiments show that this value is close to the visually observed wave height.

One can also estimate the significant wave height directly from the energy spectrum [10]:

$$Hm_0 \approx 4\sqrt{m_0} \tag{6}$$

with

$$m_0 = \int_0^\infty E(f) df$$

Observations show that the significant wave height $H_{1/3}$ is, in general, 5% to 10% lower than Hm_0, as consequence of nonlinear processes (*e.g.* wave breaking) and the fact that the model hypotheses (*i.e.* the Rayleigh distribution of the wave heights and the Gaussian distribution of the surface elevation) are not exactly verified in real waves [10].

2.1.3 Comments on the numerical formulation

As specified in [16, section 3], some of the main characteristics of the numerical approaches in WW3 are described below :

- The wave equation is solved using a fractional step method, which treats separately the temporal variations of the water depth, the intra-spectral propagation, the spatial propagation and the source term integration. This splitting scheme allows to use different time steps for each step (four different time steps can be defined by the user).
- For the spatial and the intra-spectral propagation, first, second and third-order finite volume schemes are available in WW3 and can be chosen in the compilation. For the simulations presented here, a first-order scheme is used.

2.1.4 Comments on the execution of WaveWatch III

WaveWatch III is composed by various programs, each one with a purpose in the simulation. For example, defining the problem, reading the different kinds of inputs and source terms, running the code and generating the output. In the first coupling scheme described here, without source term but with an input energy spectra imposed in a specific point, the following sequence of programs is run :

- *ww3_grid* : prepares the model problem (grid, time step, input points);
- *ww3_bounc* : reads spectra in NetCDF format and imposes them in the input points defined in *ww3_grid*;
- *ww3_shel* : performs the computation itself;
- *ww3_ounp* : produces point outputs in selected points (for example, the energy spectrum) in NetCDF format;
- *ww3_ounf* : produces field output (for example, the significant height) in NetCDF format.

2.1.5 Model's input and output

As described above, energy spectra are "natural" input and output for spectral methods such as WW3. Thus, one can easily impose and get spectra in chosen points.

2.2 BOSZ

2.2.1 Governing equations

The Boussinesq Ocean and SurfZone (BOSZ) model, developed by [17], is a dispersive nearshore wave model consisting of a Boussinesq-type system written in the conservative form of the nonlinear shallow water equations, in order to incorporate the shock-capturing capabilities of a Godunov-type scheme.

The Boussinesq system from [12], consisting of a continuity and momentum equation,

$$\begin{aligned} \eta_t + [(h+\eta)U]_x + \left[\left(\frac{z^2}{2} - \frac{h^2}{6}\right) hU_{xx} + \left(z + \frac{h}{2}\right) h(hU)_{xx}\right]_x = 0 \\ U_t + UU_x + g\eta_x + z\left[\frac{z}{2}U_{txx} + (hU_t)_{xx}\right] + \tau + R_B = 0 \end{aligned} \tag{7}$$

is reformulated to the following system, which is solved by BOSZ :

$$\mathbf{U}_t + \mathbf{F}_x = \mathbf{S} \tag{8}$$

with

$$\mathbf{U} = \begin{bmatrix} H \\ P^* \end{bmatrix}, \qquad \mathbf{F} = \begin{bmatrix} HU \\ HU^2 + \frac{1}{2}gH^2 \end{bmatrix},$$

$$\mathbf{S} = \begin{bmatrix} \psi_C \\ gHh_x + U\psi_C + \psi_M - H(\tau + R_B) \end{bmatrix}$$

$$P^* = (HU) + Hz\left(\frac{z}{2}U_{xx} + (hU)_{xx}\right), \tag{9}$$

$$\psi_M = H_t z\left(\frac{z}{2}U_{xx} + (hU)_{xx}\right) \tag{10}$$

$$\psi_C = \left[\left(\frac{z^2}{2} - \frac{h^2}{6}\right) hU_{xx} + \left(z + \frac{h}{2}\right) h(hU)_{xx}\right]_x \tag{11}$$

where $H = h + \eta$, h is the water depth and η is the free surface elevation; U is the horizontal flow velocity, z is a reference depth for the velocity computation, g is the gravitational acceleration, τ is the bottom shear stress in terms of the Manning coefficient and R_B is a parametrization of the wave-breaking characteristics.

The applicability of the model is restricted to shallow waters. In equations (9) to (11), the value of z, the reference depth to compute the velocity, depends on the water depth h and has a strong influence on the dispersion characteristics of the Boussinesq equations of [12], as remarked by [17]. BOSZ adopts the ratio $z/h = -0.53753$, determined by comparing the linear dispersion relation and the analytical solution of the linearized form of the governing equations. Numerical tests indicate that this ratio provides good dispersion properties for $0 < h/L_0 < 0.6$, where L_0 is the deep water wavelength. [17]

2.2.2 Comments on the numerical formulation

The governing equations (8) are solved using a Finite Volume scheme:

$$\frac{\partial}{\partial t}\int_\Omega \mathbf{U} d\sigma\Omega = -\frac{1}{|\Omega|}\int_\Sigma \mathbf{F} n_x d\Sigma + \int_\Omega \mathbf{S} d\Omega \tag{12}$$

where Ω and Σ are the cell domain and its boundary, and n_x is the outward normal vector. The temporal discretization is made using an explicit fourth-order predictor-corrector scheme.

The Finite Volume formulation requires the resolution of a local Riemann problem in each cell interface, in order to compute η and HU. The initial values

of these variables in the Riemann problem are computed with a fifth-order Total Variation Diminishing reconstruction scheme.

Nevertheless, numerical simulations show that this FV scheme can be highly diffusive depending on the wave properties (as we will see in the numerical tests done in this report, for which the input waves are quite nonlinear). Therefore, it is implemented in BOSZ an option that allows to discretize the hydrostatic part of (8) using an upwind Finite Difference scheme between the cells interfaces, instead of the FV scheme. In this report, both options are used and compared.

Besides these aspects, BOSZ model also has numerical features for accounting for breaking waves in the surf zone, reducing instabilities due to the frequency and amplitude dispersion in the presence of strong gradients, and sponge layers defined in both ends of the domain to avoid reflected waves.

2.2.3 Model's input: the source function method

Waves can be generated in BOSZ using a source function method, as described in [18] and [14]. This feature is explored in this project in order to impose input data for the model.

The use of this method in BOSZ, instead of the imposition of boundary conditions in single points, comes from theoretical and practical issues in using the latter approach in Boussinesq models. As remarked by [18], "the problem of generating and absorbing waves at the boundary of models based on Boussinsq-type equations is essentially an unsolved one, due to the fact that the exact structure of the well-posed initial boundary value problem is unknown for most forms of the model equations."

The source function method consists in adding source terms to the set of Boussinesq equations: a scalar source term is added to the mass balance equation, and a vector forcing term to the momentum equation.

The source terms are chosen to have a smooth Gaussian shape, so the source function covers a strictly positive width in the domain, *i.e.*, in the discrete scheme it is imposed over a range of cells. This width is computed such that the support of the source function is compact: in points sufficiently far away from the source region, the source function is negligible.

For example, in the case of the mass conservation equation, if $f = f(x, y, t)$ denotes the source function, its Fourier transform in time and direction y is imposed to be under the form

$$\hat{f}(x, \lambda, \omega) = D(\lambda, \omega) e^{-\beta x^2}$$

where the amplitude D of each spectral component satisfies the desired wave characteristics and β is a parameter that satisfies

$$e^{-\beta(x-x_s)^2} < e^{-5} \tag{13}$$

for every x outside the source region (whose center is denoted by x_s). From equation (13), we conclude that the size of the support of the source function is

$$W = 2\sqrt{\frac{5}{\beta}}$$

BOSZ accepts energy spectra as input for computing the source function, a feature that is used in our coupling scheme for taking into account the spectra

coming from WW3. In this case, the time series of the source function is computed by discretizing the frequency and the direction domains of the spectrum, computing the amplitude for each frequency and direction and then summing up their contributions using a random-phase model. Obviously, in the 1D formulation as studied here, only one direction is considered.

2.2.4 Model's output: the Welch's method

Being a time-domain model, BOSZ gives as output, for each point of the model, the timeseries of the surface elevation and the velocity. Therefore, in the coupling scheme proposed in this project (section 3), a post-treatment of this output is necessary for producing energy spectra to be used as input in WW3. As detailed later, it is done using the Welch's method.

3 The coupling scheme

The coupling between WW3 and BOSZ is made with the coupling software OpenPALM, developed at CERFACS, which allows to exchange data between different codes, synchronize them and run them in parallel.

We firstly present the initial idea for the coupling scheme, which uses the main PALM features, and some issues that forced us to modify this scheme.

3.1 Initial coupling scheme

The main characteristics of a PALM coupling are the following:

- The main program, called *palm_main*, is automatically generated by PALM and calls the coupled programs ("PALM units") as Python/C/C++ functions or Fortran subroutines;
- Each sequence of commands and units to be executed is called a "PALM branch"; multiple branches can be defined inside a PALM program and they can be executed in parallel;
- The data ("PALM objects") exchange between units is made via the interface functions *PALM_Get* and *PALM_Put* (inserted in the source code of the coupled units), analogous to the MPI point-to-point communication functions *MPI_Send* and *MPI_Recv*.

A Graphical User Interface (PrePALM) is available and allows to easily set up the branches and the communications. An example is showed in Figure 2.

In order to take advantage of the PALM features listed above, we initially intended to:

- Compile WW3 and BOSZ as functions or subroutines and call them inside PALM.
- Modify the codes of each model, inserting the PALM communication functions in order to exchange data in specific instants during the simulation;

Nevertheless, important issues prevented us from implementing this scheme:

1. **Compiling WW3 as a subroutine** : WW3 has a compiling option (named "PALM") which allows to compile the main computation program (*ww3_shel*) as a subroutine, instead of a program. We were able to compile WW3 with this option, but the execution stops while reading the model definition file generated by the grid preprocessor program (*mod_def.ww3*). Some debugging tests indicate that this is not a problem linked exclusively with PALM, because it also occurs when the WW3 subroutine is called inside a Fortran program. Apparently, considering the very few references to this compiling option in the WW3 manual and in the WW3 users' community, this option is not commonly used and this bug may have been remained unnoticed during the continuous development of the program.
2. **Integrating BOSZ in PALM** : As said above, PALM supports Python, Fortran, C and C++ functions/subroutines, but the main interfaces of BOSZ are written in Matlab.

3.2 Modified coupling scheme

In order to avoid the difficulties listed above (and considering the reduced duration of this project, which made impracticable to look for "definitive solutions", for example fully translating the BOSZ code for another language), an alternative coupling scheme was implemented.

For each one of the models, a Python function (named *interface_WW3_PALM* and *interface_BOSZ_PALM*) is used as PALM unit; in these functions, the following steps are performed:

1. Receive a synchronization flag from the other model;
2. Modify the configuration files depending on the timestep (e.g. simulation dates, names of input data files);
3. Run the model as a program via a terminal command;
4. Convert the output files to the proper format for the other model;
5. Send a synchronization flag to the other model.

In order to control the frequency of communication between the models, the total simulation is divided in partial ones, and the functions *interface_WW3_PALM* and *interface_BOSZ_PALM* are called by PALM in each partial simulation.

Figure 2 represents the structure inside PALM (a "PALM canvas") for running the proposed coupling scheme.

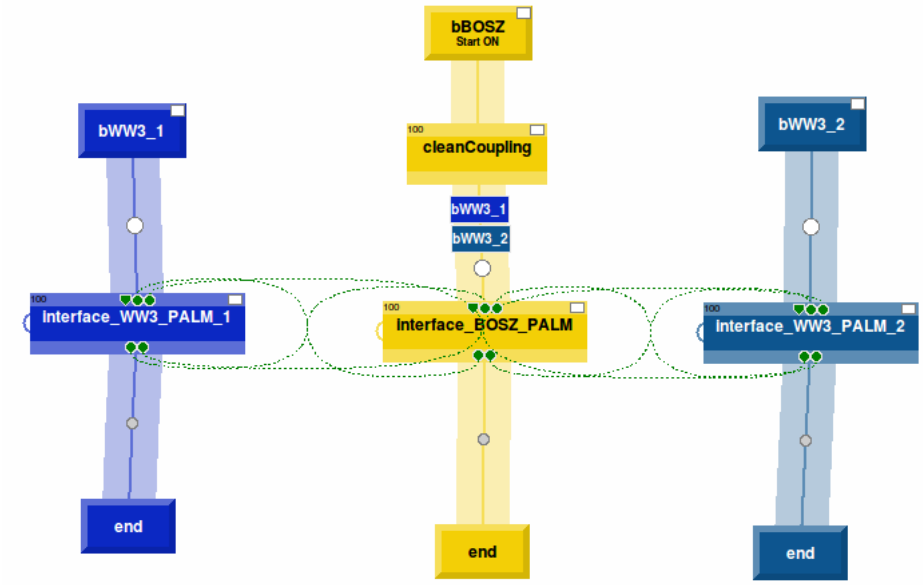

Figure 2: PALM canvas for the proposed coupling scheme. Each column is a PALM branch and calls a PALM unit (the central rectangle) for running the respective model in one of the subdomains. The green lines represent the transmission of information via the PALM interface functions (in this case, the synchronizations flags), and, in each column, the region between the white and the grey circles represent a loop over the number of partial simulations.

Some advantages and disadvantages of the proposed scheme can be listed:

Advantages:

- There is no need to modify the models' codes, since the data communication is made via input and output files and all the coding for the coupling is made in the Python interface functions;
- It is easy to produce and store intermediate results (they are the output files of the partial simulations), which can be used both for debugging and analysis of the results given by the coupling scheme.

Disadvantages:

- The models must be launched in each partial simulation, implying a higher computational time;
- At the end of each partial simulation, there is need to store the current status of execution in restart files, to be loaded in the beginning of the next partial simulation;
- All the data transmission is made via input and output files, instead of the PALM interface functions. It is a possible source of bugs, demanding a careful management of these files. Moreover, there is extra computation and storage costs.

A similar approach was adopted by [3] for coupling WW3 and the MARS3D model via PALM. Even if it is not detailed how the execution of the models is performed, the authors define intermediary Palm units in order to prepare the input variables, minimizing the modification of the source codes and allowing to an efficient computation in a supercomputer.

3.3 Data transmission through the interfaces

The main challenges for setting up the coupling scheme concerns the exchange of informations between the models. As the wave propagation is described in different ways in each model, the types of input and output data are also different, as described in the last section. Moreover, from a more practical point of view, we also have to take into account the different file formats read by the models and how the boundary conditions are defined in each software.

In a first moment, before attempting to develop more complex interface boundary conditions in the context of a domain decomposition method, we simply transmit the data through the interface at the end of each partial simulation. The information can be transmitted either from WW3 to BOSZ or from BOSZ to WW3, as detailed in the subsections below. In the first simulations it is done only in one way for each interface (from left to right), but in the next ones we will attempt to perform a communication in both ways, specially when applying domain decomposition techniques.

In each partial simulation, both models are executed in parallel, following the scheme represented in Figure 3. Details of the communications are presented below.

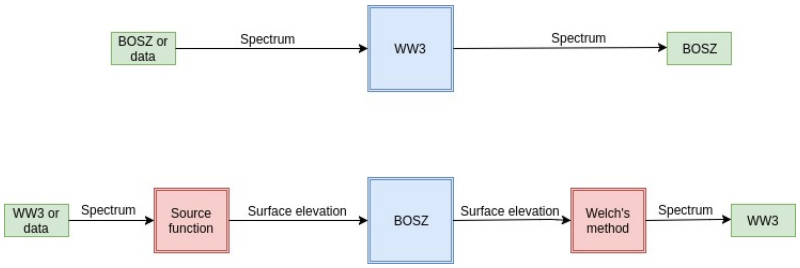

Figure 3: Scheme indicating the executions and communications performed in each partial simulation of the coupling.

3.3.1 WW3 → BOSZ

As described in paragraph 2.2.3, a Gaussian source function, covering a range of computational cells, is computed in BOSZ from an input energy spectrum.

The source function method brings additional difficulties for the purposes of this project, since we have less control over the definition of the interface boundary conditions (which is an essential aspect in the context of domain decomposition methods). Firstly, it represents an intermediary step for transmitting information between the models. As shown in the numerical simulations in the following section, in this process the input spectra is distorted, due to pretreatments for computing the source function, such as interpolations and frequency filtering. This distortion is stronger for highly nonlinear waves. Secondly, the source function cannot be implemented in a single point, as done in classical boundary conditions, and its width may vary depending on the wave properties.

In order to minimize this latter difficulty, some modifications were made in the computation of the source function inside BOSZ :

- The interface point is chosen in order to be in the center of the range of cells where the source function is defined;
- The width of the source function is chosen by the user and kept constant over the entire simulation, instead of being computed by BOSZ in the beginning of each partial simulation. The criteria (13) is verified to assure that the source function has a compact support;
- It is verified that the source region thus defined does not overlap with the sponge layers, present at both ends of the domain.

3.3.2 BOSZ → WW3

BOSZ is able to output the timeseries of the surface elevation in chosen locations. From this information, the energy spectrum can be computed via a spectral analysis [10, Appendix C].

In this project, we produce the energy spectra from the surface elevation timeseries using the Welch's method [4], which divides the timeseries in possibly

[4] https://docs.scipy.org/doc/scipy-0.14.0/reference/generated/scipy.signal.welch.html

overlapping windows, computes a spectrum for each one of them (using a Fast Fourier Transform) and averages these spectra.

This method allows to smooth the computed spectra. The number of windows and amount of overlapping is a compromise between the desired accuracy on the estimation of the spectra and the computational time. In this coupling scheme, we apply the method with ten windows, which allows a good smoothing of the spectra without high computational costs, since we perform one-dimensional tests, *i.e.*, with unidirectional spectra. A more detailed study on the influence of the number of the windows on the result is performed below.

Usually WW3 simulations are performed considering a small number of frequencies (*e.g.* 32, as in the data available for the test case presented here), defined with a logarithmic scale. As the Python function for the Welch's method returns a spectrum defined over a larger discrete frequency domain, we perform a linear interpolation of the spectra over this smaller set of frequencies.

Contrary to BOSZ, in WW3 the spectral boundary condition can be imposed in a single point.

Study on the construction of spectra using the Welch's method

In order to validate and debug the application of the Welch's method to construct energy spectra from surface elevation timeseries, and also to study the influence of the number of frequency windows used in this method, a simple test is presented here.

From an energy spectrum (the initial input spectrum of the test case presented in Section 4), we compute a surface elevation timeseries with random phase, within a certain time window. Then, from this timeseries, we use the Welch's method to reconstruct the energy spectrum and compare it with the original one, since we expect them to be similar.

As described above, the Welch's method returns a spectrum defined over a large discrete set of frequencies, but is mainly concentrated in the frequency range considered in the models' computations. Therefore, we interpolate the spectrum to this smaller frequency set, and we rescale it in order to have the same integral of the non interpolated spectrum.

Figure 4 to 6 present the study performed with timeseries computed using different numbers of timesteps. In all the cases, the timestep is kept constant ($\Delta t = 1s$) and the final instant varies.

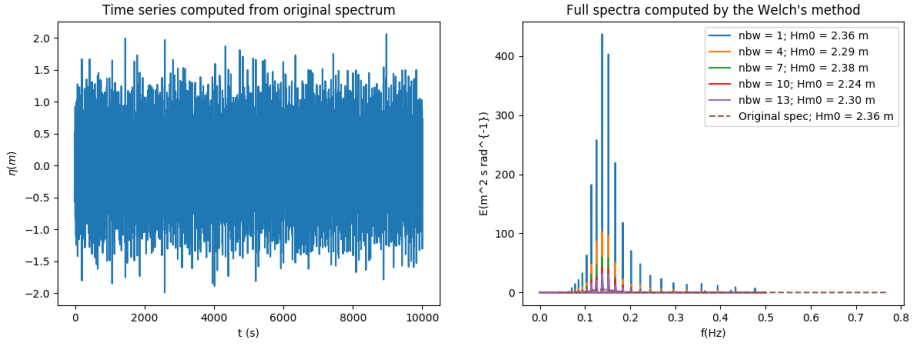

(a) Time series (b) Full spectra computed by the Welch's method

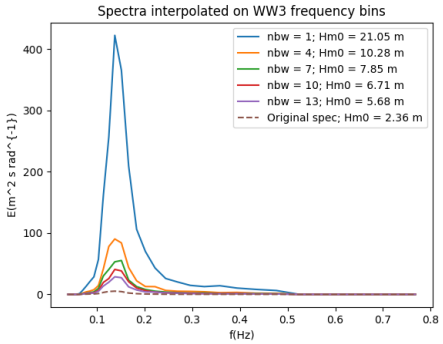

(c) Interpolated spectra

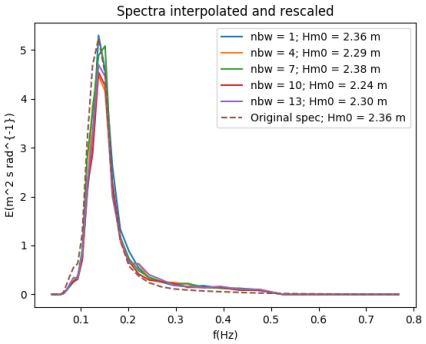

(d) Interpolated and rescaled spectra

Figure 4: Study of the application of the Welch's method, with a timeseries computed with 10000 timesteps, for different numbers of windows (nbw). The estimation Hm_0 of the significant height is computed for each spectrum

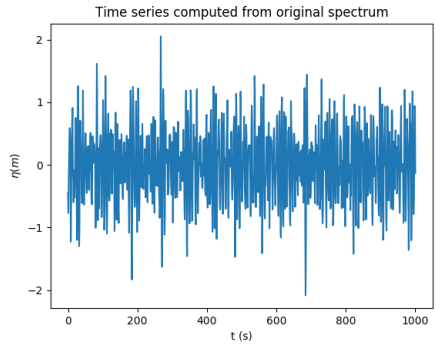

(a) Time series

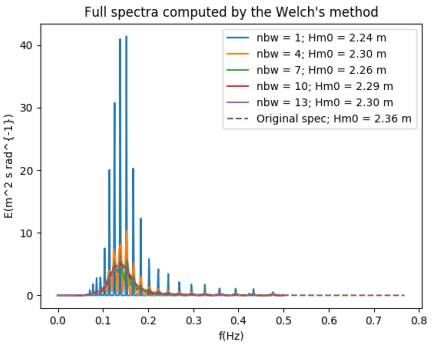

(b) Full spectra computed by the Welch's method

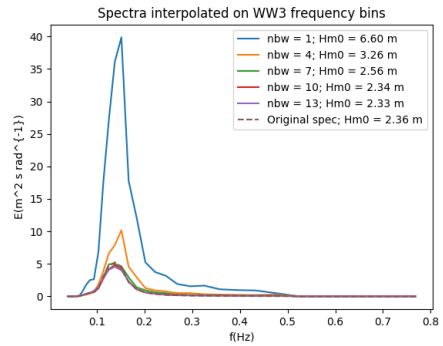

(c) Interpolated spectra

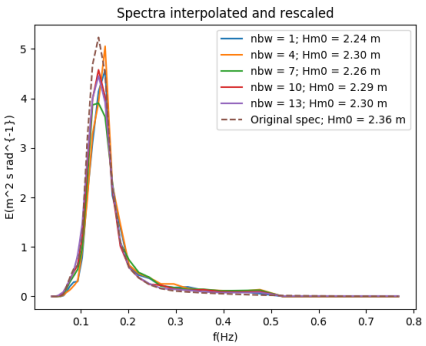

(d) Interpolated and rescaled spectra

Figure 5: Study of the application of the Welch's method, with a timeseries computed with 1000 timesteps, for different numbers of windows (nbw). The estimation Hm_0 of the significant height is computed for each spectrum

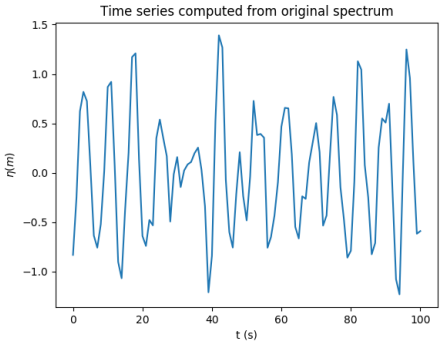

(a) Time series

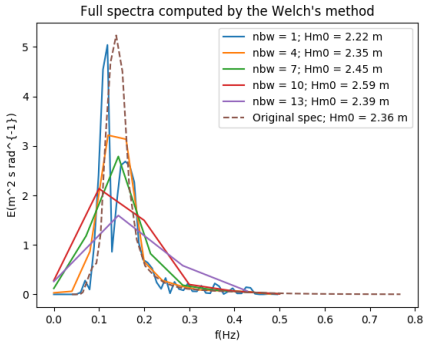

(b) Full spectra computed by the Welch's method

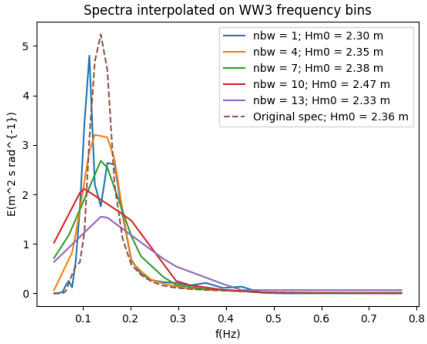

(c) Interpolated spectra

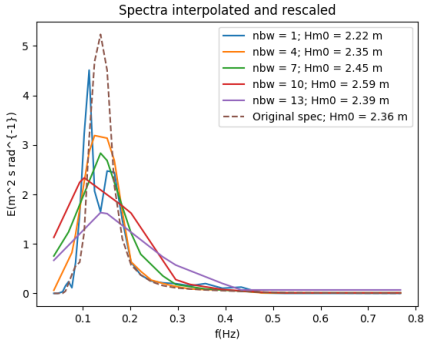

(d) Interpolated and rescaled spectra

Figure 6: Study of the application of the Welch's method, with a timeseries computed with 100 timesteps, for different numbers of windows (nbw). The estimation Hm_0 of the significant height is computed for each spectrum

As a conclusion of the results presented above, we do not observe a direct relation between the number of windows and the quality of the reconstructed spectrum when the timeseries is large enough. Nevertheless, when it has few time steps, there is no sufficient data to produce good estimations of the energy spectrum; in this case, the smoothing obtained when using more windows in the Welch's method becomes more evident, but it causes a reduction of the energy peak.

4 1D test case - Guérande sandbank

4.1 Description of the test case

The one-dimensional test case solved here consists in the flow propagation over a sandbank near Guérande, in the Atlantic coast of France.

The domain has a total length of $45126m$, divided with a homogeneous mesh size $\Delta x \approx 4.56m$, totalizing 9901 discrete points. As represented in Figure 7, it was divided in three subdomains, accordingly to the bathymetry profile. In the outer domains, where the depth is higher than 18 m, the flow is modeled by WW3; in the central domain, containing the sandbank, the BOSZ model is used. There is a small overlap between the domains (20 cells around each interface), resulting in the following number of points for each subdomain:

- WW3 (left) : 5164 points
- BOSZ : 877 points
- WW3 (right) : 3900 points

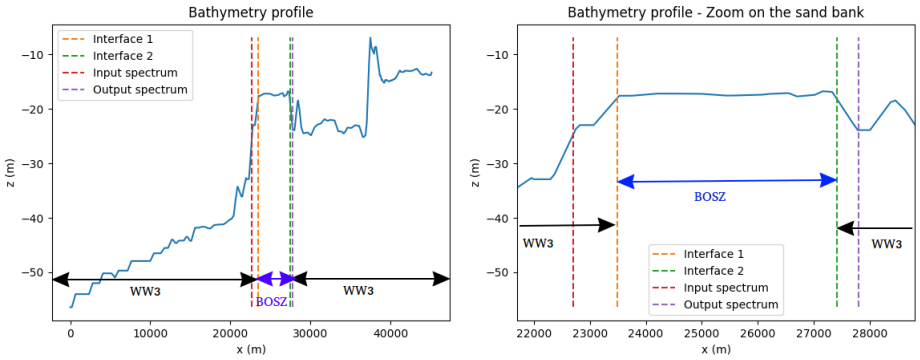

(a) General view

(b) Zoom on the sandbank

Figure 7: Computational domain

We perform a simulation with a total run time of 3000 seconds, divided in 5 partial simulations of 600 seconds, with the following timesteps :

- $\Delta t_{WW3} = 0.15s$
- $\Delta t_{BOSZ} \approx 0.02s$, obtained imposing the CFL condition 0.4

These timesteps were chosen after some initial tests, in order to avoid instabilities of the models.

The available input data consist in a set of energy spectra at $x \approx 22700m$ (represented in the Figure 7 as the vertical line labeled as "Input spectrum"), in the beginning of the sand bank. The spectra are defined every 30 min for the month of February 2014. As the spectra on the first hour (the time window for the simulation performed here) don't differ significantly, only the initial spectrum is considered.

The data also contain output spectra at $x \approx 27805m$, in the exit of the sand bank (the line "Output spectrum" in Figure 7). These spectra are used here as a reference solution: the results obtained after $3000s = 50min$ are compared to the linear interpolation of the spectra at $30min$ and $1h$. The reference spectra are not real ones, but were computed in a 2D WW3 simulation in the same area. This 2D simulation is characterized by the fact that transversal flows are negligible, so we can expect the 1D simulation to give similar results.

The input and output spectra are represented in Figure 8.

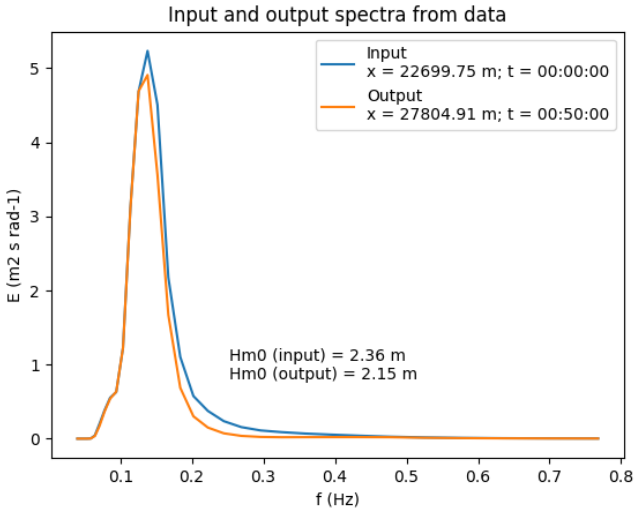

Figure 8: Input and output spectra from data

When defining the subdomains, we took into account not only the water depths, but we also intended to have similar computational times in all the PALM branches. Therefore, the WW3 subdomains have similar sizes and are significantly bigger than the BOSZ subomain, due to the different order of magnitude of the time steps in each model.

As a consequence, the left WW3 subdomain was defined with the input point very close to the right boundary. We remark that computations are made in the left of the input point, but the results in the region do not have a physical meaning, as the input spectra propagates from off-shore to the coast.

4.2 Verification of the range of validity of the BOSZ model

A brief analysis is presented in the following paragraphs for estimating the range of validity of the input spectra in the BOSZ model, considering, as said above, that its parameters were chosen such that the model gives good results with the water depth verifying $0 \leq h/L_0 \leq 0.6$, where L_0 is the deep water wavelength.

We need firstly to estimate the deep water wavelength. For that, we use some statistical definitions of characteristic frequencies of the spectrum, following [10, chapter 4]:

- The peak frequency f_{peak}, which is, accordingly to empirical observations,

approximately equal to the significant wave frequency $f_{1/3,swell}$ in the case of swell (*i.e.*, waves with a narrow spectrum);

- The significant wave frequency for wind sea, $f_{1/3,wind} \approx 1/0.95 f_{peak}$;
- The mean frequency $f_{mean} = m_1/m_0$;
- The mean frequency of the level crossing, for a surface elevation η : $\overline{f}_\eta = \sqrt{m_2/m_0}\exp\left(-\eta^2/(2m_0)\right)$

where m_n refer to the m-th order moment of the spectrum:

$$m_n = \int_0^\infty f^n E(f) df \tag{14}$$

For each of these frequencies, and for values of depth going from 10 to 1000 meters, the dispersion relation (4) was solved iteratively, using the bisection method, in order to get the wavelength L. Figure 9 illustrates the results, showing a convergence of the wavelength for higher values of the water depth. The converged values were adopted as the deep water wavelength L_0.

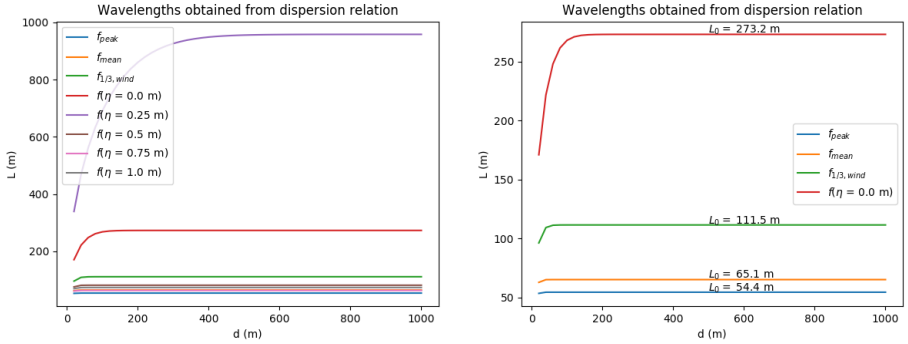

(a) Overall results

(b) Detail for some frequencies

Figure 9: Computed of wavelength for various characteristic frequencies of the input spectrum Right figure shows some of the curves with the respective converged value of L_0.

Finally, Figure 10 presents, for each of the computed frequencies, the ratio h/L_0 for $h \leq 60m$; which covers approximately the range of depths in this test case. We observe that the depth range in which the BOSZ model is defined in the coupling scheme ($h \leq 18m$) is inside its domain of validity.

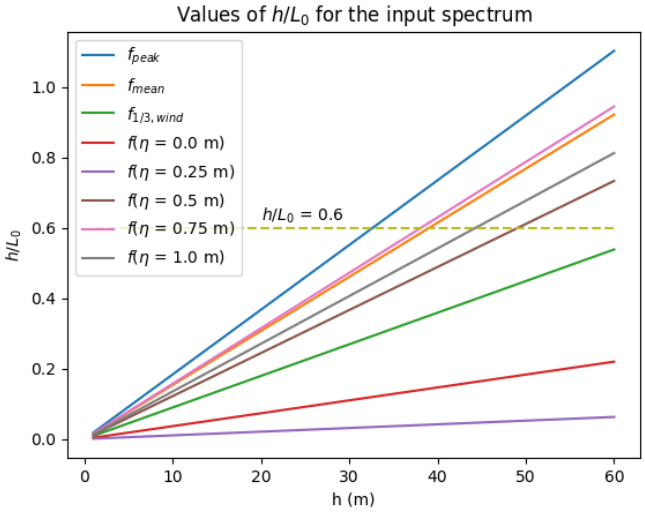

Figure 10: Ratio h/L_0 for each frequency considered

4.3 Results

Numerical simulations were performed using both the coupling scheme and each of the models in the entire domain. For analyzing the results, we compare the spectra obtained in the output point in the end of simulation (after 3000 seconds), and also the reference spectrum available in the data. This comparison is both qualitative (deformation of the spectrum, position and height of the peak energy) and quantitative (Hm_0).

We emphasize that we do not expect all the simulations to give similar results, since the models solve different governing equations and have different properties and assumptions. Furthermore, we recall that our "reference solution" is not a real one, but the result of a 2D WW3 simulation (thus, we expect the solution given by 1D WW3 to be similar, even if it is not necessarily a physically good solution).

4.3.1 Full WW3 simulation

Figure 11 presents the computed spectrum in the output point, at the end of the simulation, compared to the reference spectrum in the same point and instant and the input spectrum used in the beginning of the simulation. As expected, the computed and the "reference solution" are very close. We can observe that the peak energy is similar in the computed and the reference spectra, showing a similar decay for this frequency, but for higher frequencies the shape of the computed spectrum is better conserved regarding to the input one. As a consequence, it has a higher Hm_0 than the reference spectrum. Besides these small remarks, we can conclude that, in this test case, the 1D WW3 simulation is a good approximation for the 2D WW3 one.

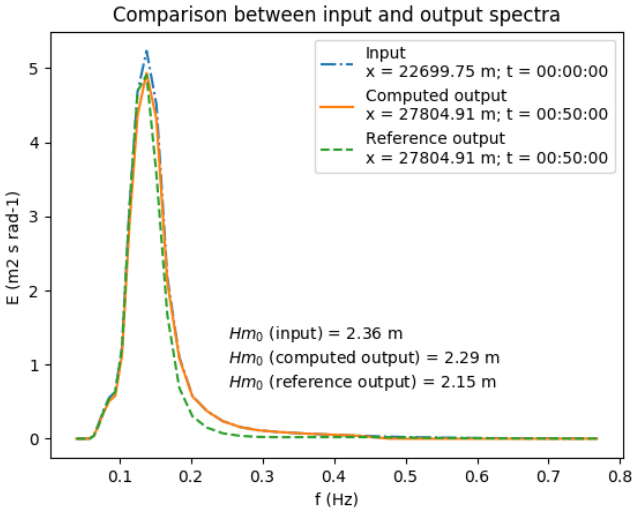

Figure 11: Comparison between input and output (computed and reference spectra)

4.3.2 Full BOSZ simulation using the FV discretization for the fluxes

As described in Section 2.2, the hydrostatic part of the governing equation (8) can be discretized both with FV or FD schemes. We firstly present the results with the FV discretization.

Timeseries output data can be obtained in BOSZ by putting "gauges" in choses points. Some of the gauges positioned on the domain are represented in Figure 12, including the input and output point (gauges 7 and 9).

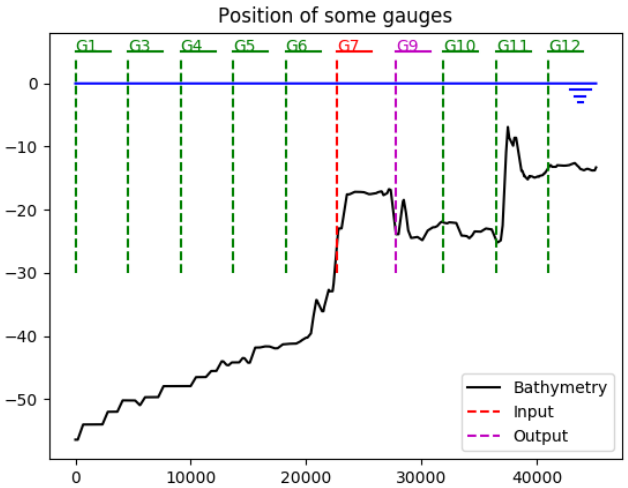

Figure 12: Some of the gauges positioned on the domain. Emphasys on the ones on the input and output points

Figure 13 represents the timeseries of the surface elevation for some of the selected points, including the input point (gauge 7) and the output point (gauge 9). In these figures, we can observe the propagation of the spectra from the input point, since the time series in the farthest points start to be non-zero only after some time. We can also observe a strong damping of the energy.

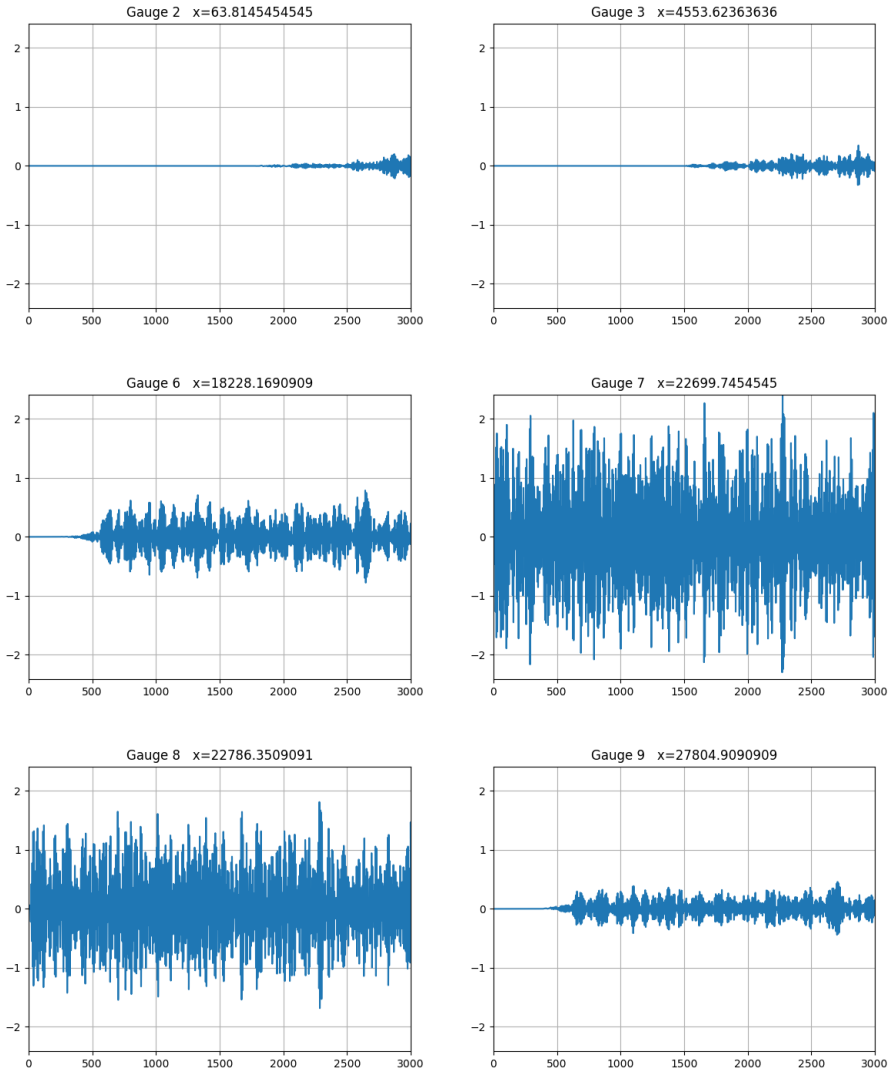

Figure 13: Time series of the surface elevation for some points. Gauge 7 and 9 are respectively the input and output points. Results obtained using the FV scheme in BOSZ

The energy damping can also be observed in the spectra computed from the timeseries, as represented in Figure 14, for the same gauges. For each graph, we plot the Hm_0 computed from the original spectra obtained by the Welch's method and the one computed from the spectra interpolated to the

frequencies values used in WW3 (showing that the there is not an important loss of information in this process since the non interpolated spectra is mainly concentrated in the WW3 frequency range).

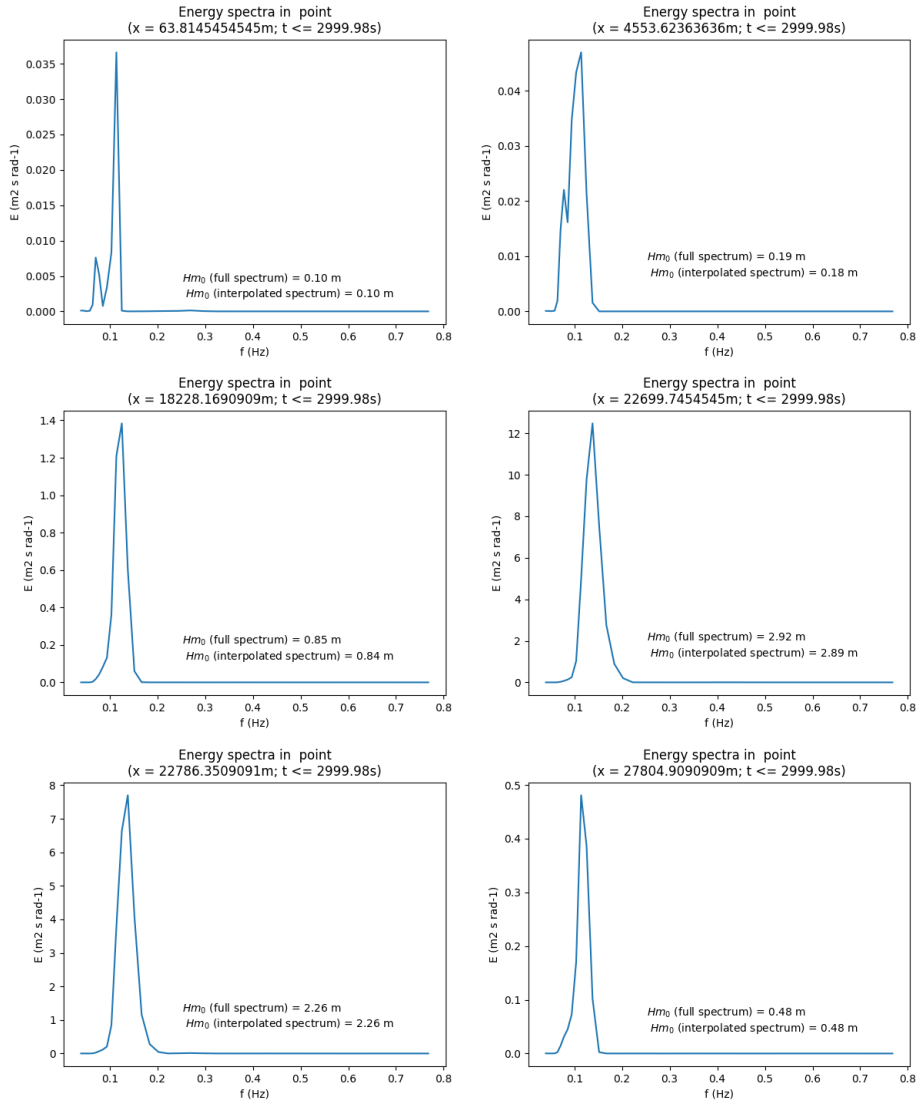

Figure 14: Energy spectra for some points. Gauge 7 and 9 are respectively the input and output points. Results obtained using the FV scheme in BOSZ

4.3.3 Full BOSZ simulation using the FD discretization for the fluxes

We present in Figures 15 and 16 the same results as above, but with the FD discretization for the hydrostatic part of (8). As discussed above, as the input wave is highly nonlinear, the numerical damping with this new discretization is much smaller than the one verified with the FV scheme.

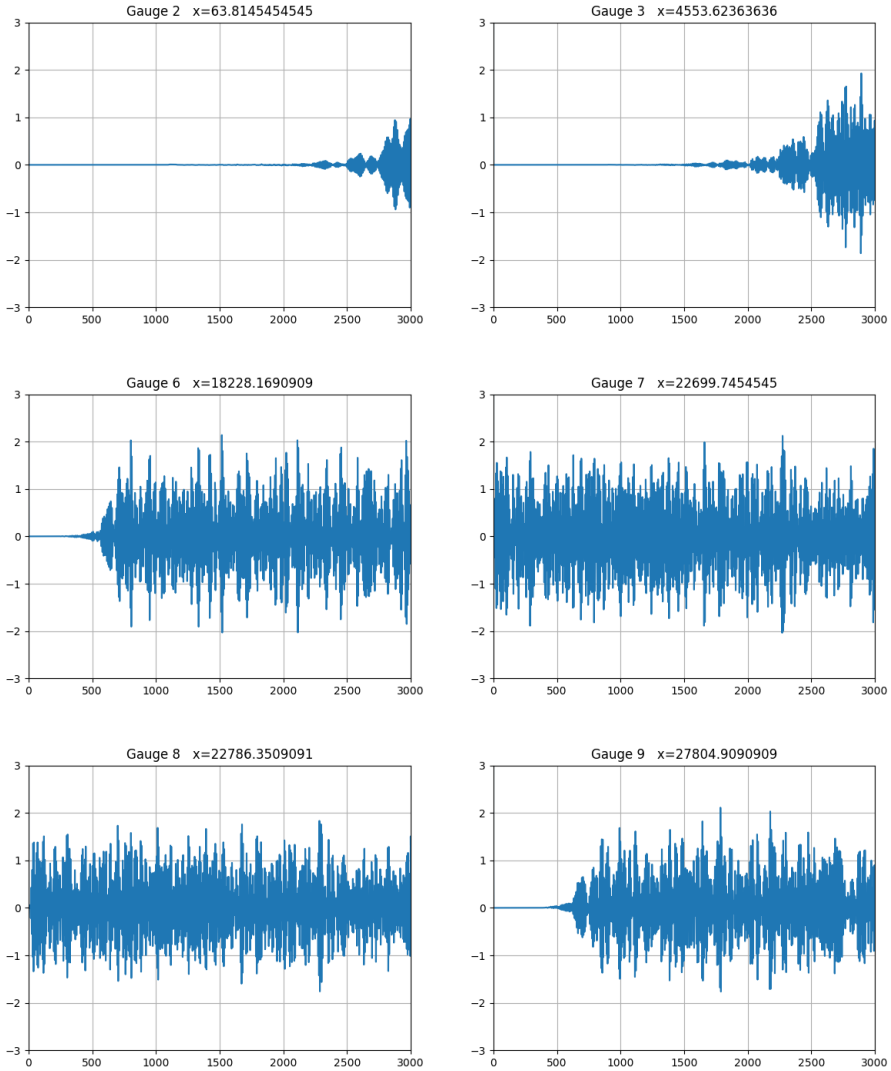

Figure 15: Time series of the surface elevation for some points. Gauge 7 and 9 are respectively the input and output points. Results obtained using the FD scheme in BOSZ

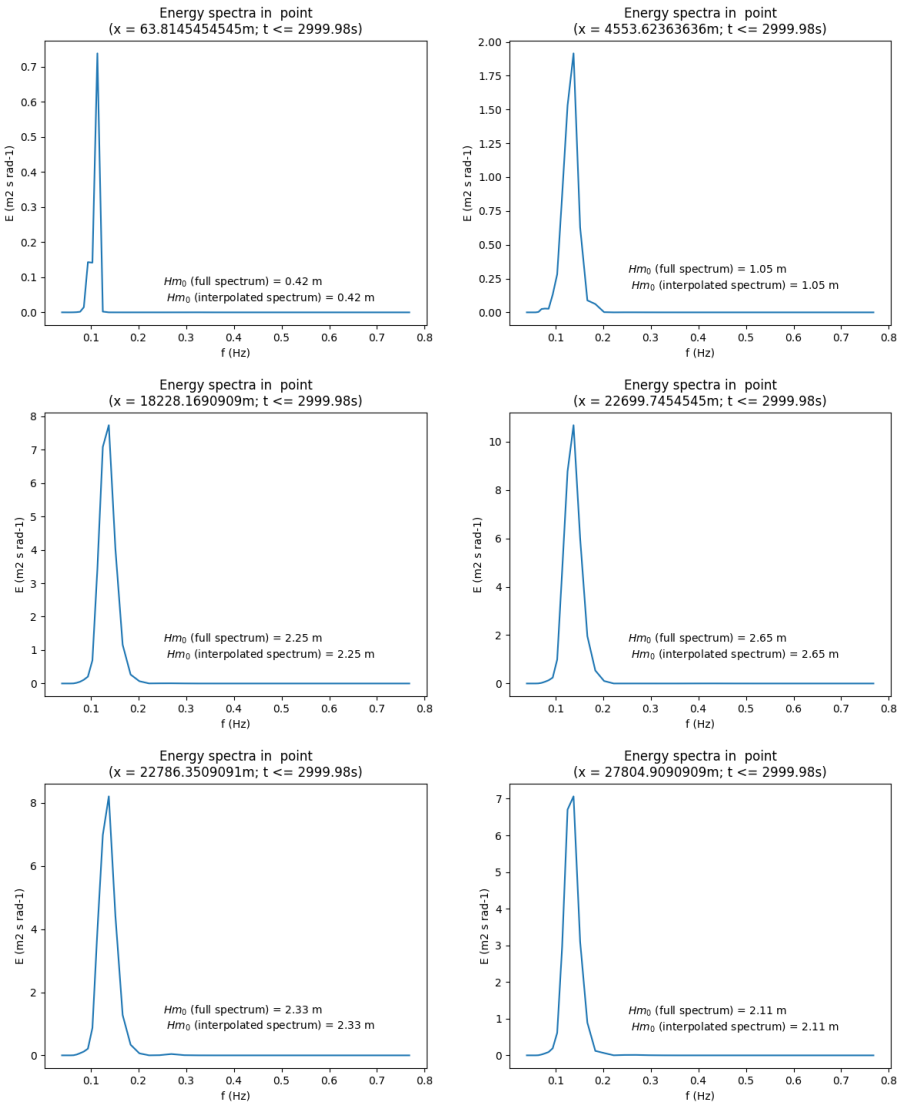

Figure 16: Energy spectra for some points. Gauge 7 and 9 are respectively the input and output points. Results obtained using the FD scheme in BOSZ

Deformation of the output spectra due to the source function method

In order to verify how the input spectra are incorporated into BOSZ via the source function method, we placed a gauge in the input point (as shown in Figure 12), in order to get the timeseries in the same point where the input data is imposed. Using the Welch's method, the spectra is reconstructed from the timeseries. We expect to obtain similar spectra. Figure 17 compares these spectra, showing that they are deformed, with a stronger concentration of the energy around the peak frequency, resulting in higher values of Hm_0. The fact that the deformation is not the same when using the FV or the FD schemes possibly results from flow computations inside the source region.

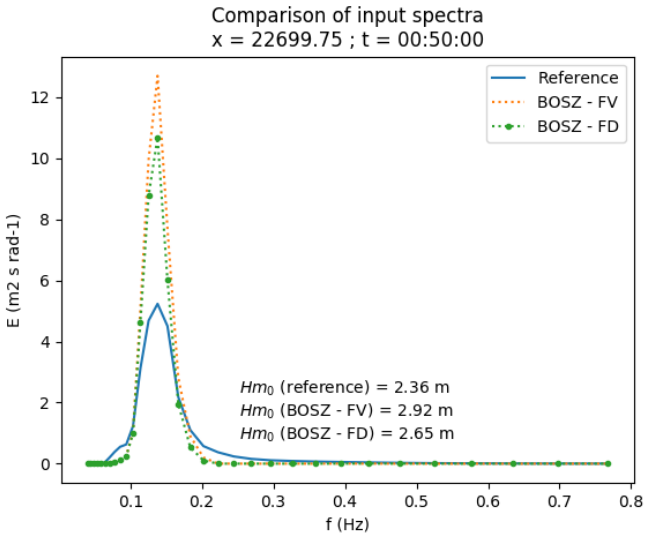

Figure 17: Comparison of the input spectra from data and the spectra obtained, in the same point, from the time series produced by the source function method

4.3.4 Coupled simulation

Before comparing the results of the coupled simulation with the previous ones, we present, step-by-step, the propagation of the solution through the coupling model, *i.e.*, we show the information transmitted between the subdomains.

Figure 18 presents the evolution of the energy spectrum that is transmitted from the left WW3 domain to the BOSZ domain. We can see that after 10 minutes of simulation the information to be transmitted has already reached the interface point and thus converged, which is a consequence of the closeness between this point and the one where the spectra from the data is imposed.

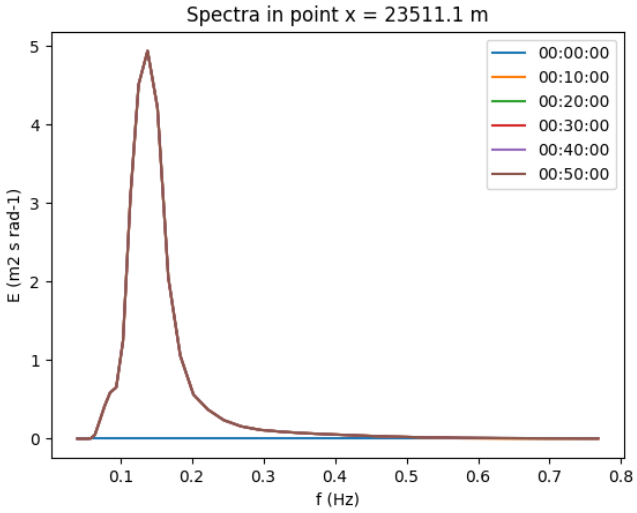

Figure 18: Evolution of the spectrum in the interface between the left WW3 domain and the BOSZ domain. Except for the first time step represented, all the spectra overlap

Figure 19 and 20 (corresponding respectively to BOSZ with FV and FD schemes for the fluxes) presents the times series of the surface elevation for some points, including the interface with the left WW3 domain (gauge 2), *i.e.*, where it is defined the input spectrum for BOSZ, and the interface with the right WW3 domain (gauge 8), *i.e.*, where the spectra is transmitted from BOSZ.

In these figures, as expected, we can observe that, for the first partial simulation ($t \leq 600s$), the surface elevation is zero for all the points, because no information has come from the left WW3 domain. As in the full BOSZ simulation, we observe a strong damping of the energy in the case of the FV discretization.

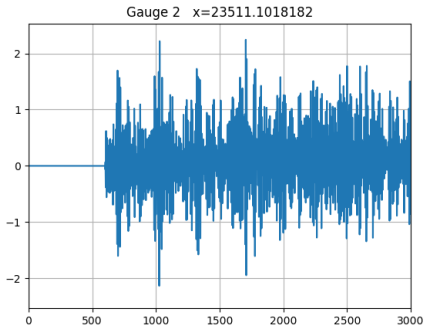

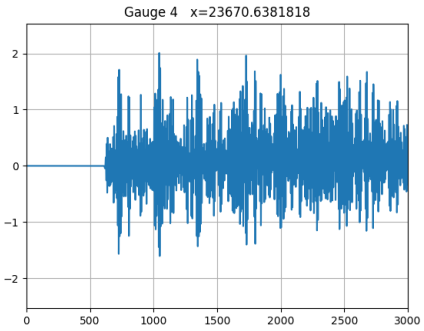

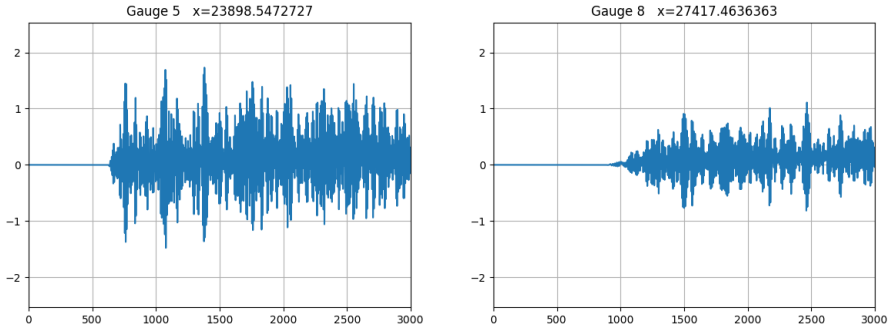

Figure 19: Time series of the surface elevation for some points. Gauge 2 and 8 are respectively the input and output points for the left and right WW3 domains. Results obtained using the FV scheme in BOSZ

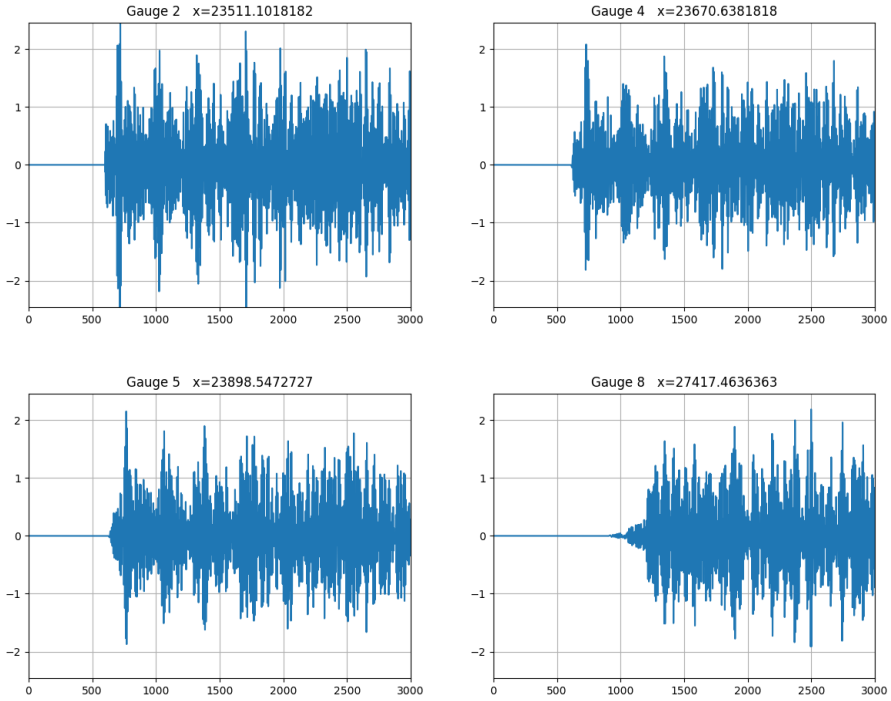

Figure 20: Time series of the surface elevation for some points. Gauge 2 and 8 are respectively the input and output points for the left and right WW3 domains. Results obtained using the FD scheme in BOSZ

The spectra for these points are presented in Figures 21 and 22.

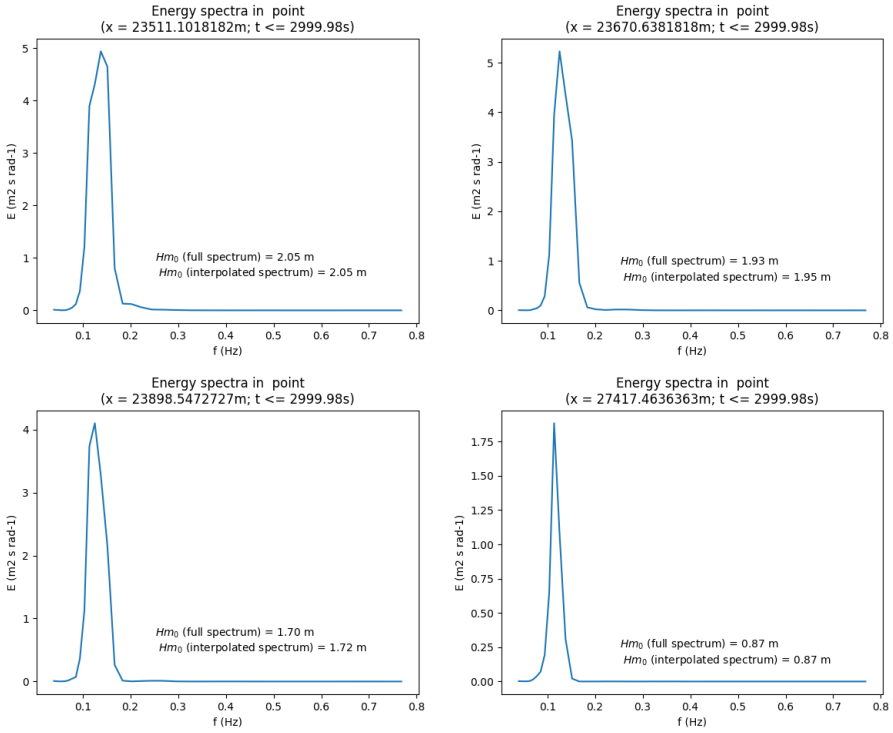

Figure 21: Energy spectra for some points. Gauge 2 and 8 are respectively the input and output points for the left and right WW3 domains. Results obtained using the FV scheme in BOSZ

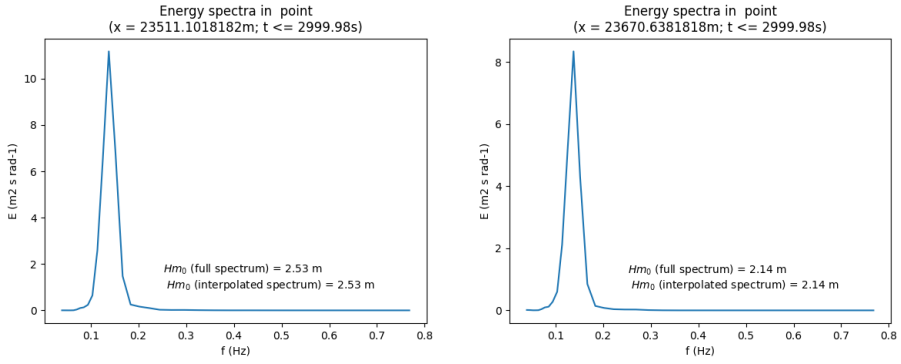

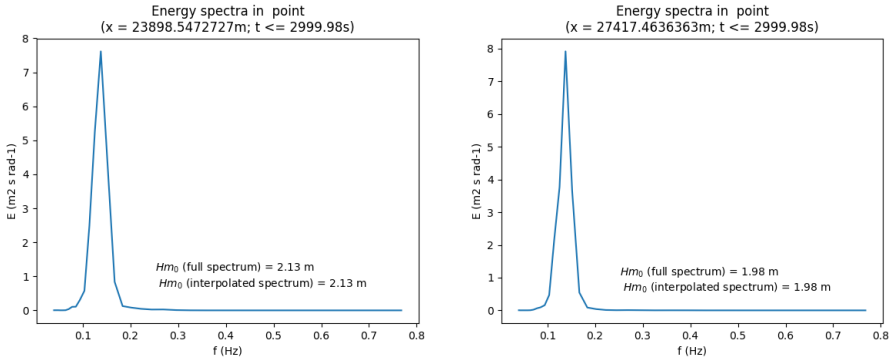

Figure 22: Energy spectra for some points. Gauge 2 and 8 are respectively the input and output points for the left and right WW3 domains. Results obtained using the FD scheme in BOSZ

Figure 23 presents the evolution of the spectra in the output point (in the right WW3 subdomain), and also the evolution of Hm_0. In the end of the total simulation, the output spectrum has not yet converged, showing that information has not been fully transported through the BOSZ subdomain.

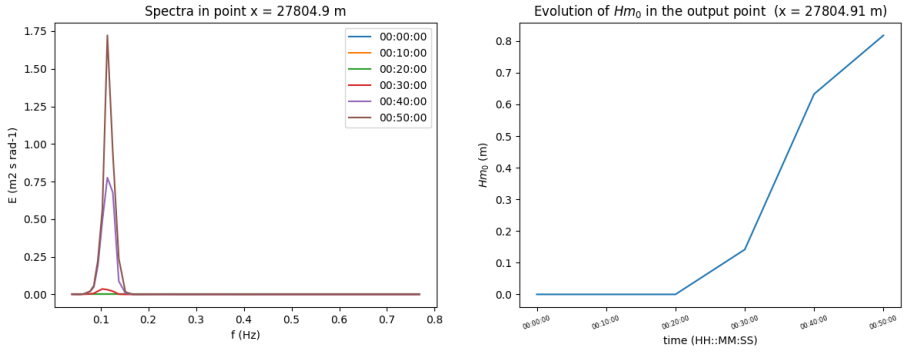

(a) Evolution of the spectra

(b) Evolution of Hm_0

Figure 23: Evolution of the spectra in the output point. Results obtained using the FV scheme in BOSZ

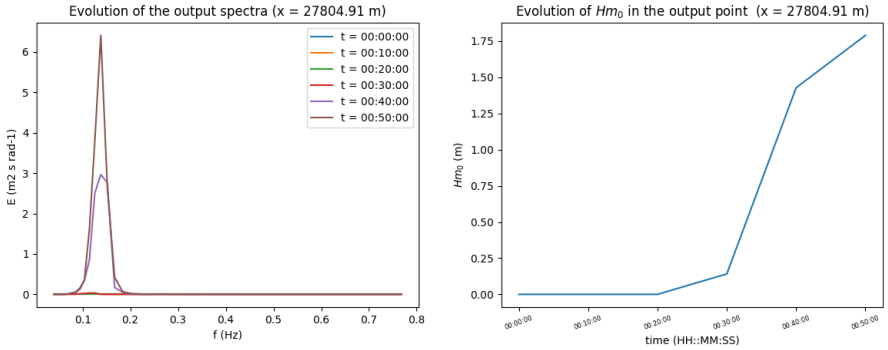

(a) Evolution of the spectra

(b) Evolution of Hm_0

Figure 24: Evolution of the spectra in the output point. Results obtained using the FD scheme in BOSZ

4.4 Comparison between all the simulations

To resume the results of this first set of simulations, Figure 25 and 26 compare the spectra obtained after 50 minutes in the output point (respectively with FV and FD schemes in BOSZ).

In the FV case, we can see that the energy damping of the coupling model is intermediary between the ones verified in the full WW3 and BOSZ simulations.

In the FD case, on the other hand, the damping still exists but is much less important, as one can see by the values of Hm_0. For this reason, the initial deformation of the spectrum, due to the source function, remains remarkable, so in the simulations using BOSZ the peak energy of the output spectra is higher.

As a final remark, contrary to the FV case, in the FD case the output spectra for the coupled simulation is not intermediary between the full WW3 and full BOSZ simulations, what is not necessary surprising since the source function acts over different spectra: in the coupling case, this spectra is the one coming from the left WW3 domain; in the full BOSZ case, it is over the data input spectrum.

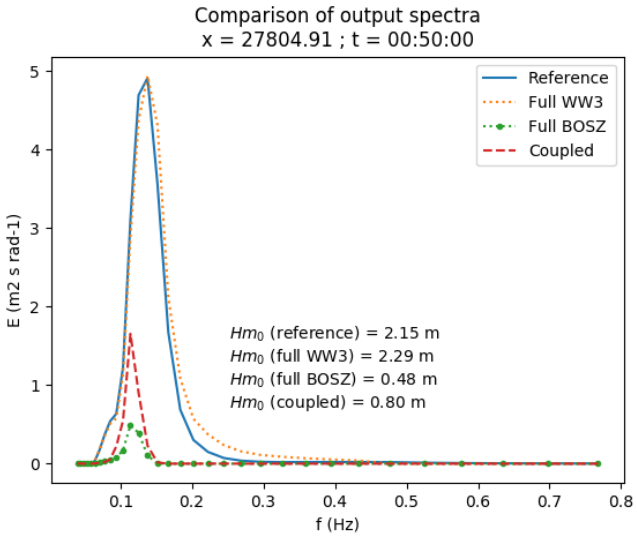

Figure 25: Comparison between the output spectra off all the simulations. Results obtained using the FV scheme in BOSZ

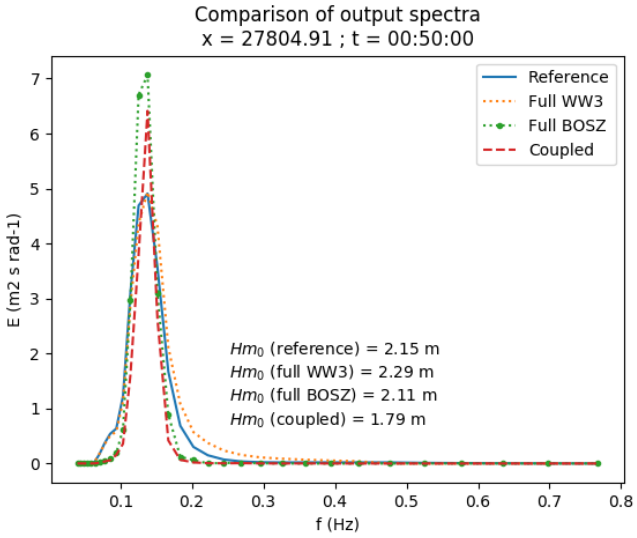

Figure 26: Comparison between the output spectra off all the simulations. Results obtained using the FD scheme in BOSZ

4.5 Conclusions on the simulations

The coupling scheme constructed for the simulations presented in this section is very simple. Indeed, in this first moment we did not attempt to improve the interface boundary conditions between the models, and we simply made the information to be transmitted along all the domain. The main idea here was to set up a base coupling scheme for future work. As a result of this initial work, it can be easily adapted for other testcases, and even changing the Boussinesq

model (as we may do depending on the type of boundary conditions to be used) or moving to 2D simulations shall not present great difficulties.

For the same reasons, the "validation tests" had the objective of verifying the good behavior of the scheme in a computational point of view. Due to the absence of real validation data, we could not physically evaluate the simulation.

5 Study on transparent boundary conditions for BOSZ

The work presented until here consisted mainly on setting up a coupled simulation between WW3 and BOSZ, and the focus was on solving the several numerical aspects necessary to their synchronization and correct exchange of information. We did not seek to improve the boundary conditions: we simply aimed to pass the information from one model to the other, from the off-shore to the nearshore zone.

In this section, we present initial studies for improving the interface boundary conditions in the coupling scheme. As said previously, the generation and absorption of waves at the boundaries of Boussinesq-type models is an unsolved problem; in practice, this fact results on the using of a source function method and sponge layers in BOSZ model [17], reducing the control over the boundary conditions.

Therefore, we want to find approximate transparent boundary conditions (TBCs) for the governing equations of the BOSZ model. TBCs are defined such that the solution of a problem calculated in a finite computational domain Ω coincide with the solution of the entire space, restricted to Ω. Nevertheless, TBCs are in general non local in time and space, so their exact computation is not doable both analytically and numerically. Therefore, one needs to approximate them in order to have an efficient numerical implementation [1].

We study here the TBCs for the linearized form of BOSZ governing equations. Even in this case, the TBCs must be computed in an approximated way.

5.1 Linearization of the governing equations

We revisit the 1D Boussinesq-type equations of [12] (which were reformulated by [17] to derive the equations solved in BOSZ model):

$$\begin{aligned} \eta_t + [(h+\eta)U]_x + \left[\left(\frac{z^2}{2} - \frac{h^2}{6}\right) hU_{xx} + \left(z + \frac{h}{2}\right) h(hU)_{xx}\right]_x = 0 \\ U_t + UU_x + g\eta_x + z\left[\frac{z}{2}U_{txx} + (hU_t)_{xx}\right] + \tau + R_B = 0 \end{aligned} \tag{15}$$

For this initial study, we work on a simplified framework, without bottom shear stress and wave-breaking parametrization (respectively by taking $\tau = 0$ and $R_B = 0$). We also consider a flat bottom ($h = h_0$) and we perform a linearization of equation (7):

$$u = u_0 + u', \qquad \eta = \eta_0 + \eta' \tag{16}$$

around the mean values u_0 and $\eta_0 = 0$. By definition of the total water depth,

$$H = h + \eta = h_0 + \eta \tag{17}$$

Replacing (16) and (17) into (7), adding initial and boundary conditions and, for sake of clarity, dropping the prime, we have

$$\begin{cases} \eta_t + h_0 u_x + u_0 \eta_x + \left(\dfrac{z^2}{2} + h_0 z + \dfrac{h_0^2}{3}\right) h_0 u_{xxx} = 0 & \text{in } \Omega \quad (18a) \\ u_t + u_0 u_x + g\eta_x + z\left(\dfrac{z}{2} + h_0\right) u_{xxt} = 0 & \text{in } \Omega \quad (18b) \\ X = \Upsilon & \text{on } \partial\Omega \quad (18c) \\ X(\cdot, 0) = X^{ini} & \text{in } \Omega \quad (18d) \end{cases}$$

with $X(x,t) = (\eta(x,t), u(x,t))^T$.

5.2 Derivation of an optimized Schwarz method

In order to derive approximated TBCs for (18a)-(18d), we follow the work of [5] and [6] and develop the resolution of this problem using a domain decomposition method (DDM). We split the computational domain Ω in two possibly overlapping subdomains Ω_1 and Ω_2, with $\Omega = \Omega_1 \cup \Omega_2$ and the interfaces

$$\Gamma_1 = \partial\Omega_1 \cap \Omega_2, \qquad \Gamma_2 = \partial\Omega_2 \cap \Omega_1$$

We implement here an additive Schwarz method (ASM), which consists in an iterative method. Denoting by $X_j^k = (\eta_j^k, u_j^k)$ the solution in the subdomain Ω_j in iteration k, the problem to be solved in Ω_j is

$$\begin{cases} \mathcal{L}_{lin}\left(X_j^k\right) = 0 & \text{in } \Omega_j \times \mathbb{R}^+ \quad (19a) \\ X_j^k = \Upsilon & \text{on } \partial\Omega_j \backslash \Gamma_j \times \mathbb{R}^+ \quad (19b) \\ \text{IBC} & \text{on } \Gamma_j \times \mathbb{R}^+ \quad (19c) \\ X_j^k(\cdot, 0) = X_j^{ini} & \text{in } \Omega_j \quad (19d) \end{cases}$$

where

$$\begin{aligned} \mathcal{L}_{lin} : \left(\Omega \times \mathbb{R}^+\right)^2 &\longrightarrow \mathbb{R}^2 \\ (\eta, u) &\longmapsto \begin{pmatrix} \eta_t + h_0 u_x + u_0 \eta_x + \tilde{h} u_{xxx} \\ u_t + u_0 u_x + g\eta_x + \overline{h} u_{xxt} \end{pmatrix} \end{aligned}$$

and

$$\tilde{h} = \left(\frac{z^2}{2} + h_0 z + \frac{h_0^2}{3}\right) h_0, \qquad \overline{h} = z\left(\frac{z}{2} + h_0\right)$$

The symbol Υ indicates the external boundary conditions and IBC indicates the Interface Boundary Conditions to be defined between the subdomains, and which characterize the DDM. We want to define the IBCs that provide the fastest convergence of the method towards the exact solution of the same problem solved in the monodomain Ω; the fact that such optimal conditions are exactly the perfectly TBCs [11] is what motivates us to study the TBCs for (18a)-(18d) via the construction of a DDM.

In order to determine the shape of the IBCs, we derive the *natural transmission conditions*, *i.e.*, the quantities that are naturally preserved through Γ_j. For this, we write (18a)-(18b) in the conservative form:

$$\eta_t + \left(h_0 u + u_0 \eta + \tilde{h} u_{xx}\right)_x = 0$$
$$u_t + \left(u_0 u + g\eta + \overline{h} u_{xt}\right)_x = 0$$

which shows that the natural transmission conditions are

$$\begin{pmatrix} h_0 u + u_0 \eta + \tilde{h} u_{xx} \\ u_0 u + g\eta + \overline{h} u_{xt} \end{pmatrix}$$

Thus, the IBCs for the ASM have the generic form

$$\mathcal{B}_j(X_j^k) = \mathcal{B}(X_{j'}^{k-1}) \qquad \text{on } \Gamma_j \tag{20}$$

where $j' \neq j$ and the operator $\mathcal{B}_j$ is defined as

$$\mathcal{B}_j(X) = n_j \begin{pmatrix} h_0 u + u_0 \eta + \tilde{h} u_{xx} \\ u_0 u + g\eta + \overline{h} u_{xt} \end{pmatrix} - S_j X$$

where $n_j = (-1)^{j+1}$ (indicating the outward normal vector to the interface, *i.e.*, the positive or negative direction x) and $S_j \in \mathbb{C}^{2\times 2}$ is a generic operator to be defined. In the optimal DDM, S_j is called the *Dirichlet-to-Neumann operator* and is defined by [6]

$$\begin{aligned} S_j : \left(\Gamma_j \times \mathbb{R}^+\right)^2 &\longrightarrow \mathbb{R}^2 \\ (\eta^b, u^b) &\longmapsto n_j \begin{pmatrix} h_0 \breve{u} + u_0 \breve{\eta} + \tilde{h} \breve{u}_{xx} \\ u_0 \breve{u} + g\breve{\eta} + \overline{h} \breve{u}_{xt} \end{pmatrix}\Bigg|_{\Gamma_j} \end{aligned}$$

where $\breve{X} = (\breve{\eta}, \breve{u})$ is the solution of the following problem, solved in the complementary set of Ω_j, denoted by Ω_j^c, with (η^b, u^b) as Dirichlet boundary condition on Ω_j:

$$\begin{cases} \mathcal{L}_{lin}\left(\breve{X}\right) = 0 & \text{in } \Omega_j^c \times \mathbb{R}^+ & \text{(21a)} \\ \breve{X} = \Upsilon & \text{on } \partial\Omega_j^c \backslash \Gamma_j \times \mathbb{R}^+ & \text{(21b)} \\ \breve{X} = (\eta^b, u^b) & \text{on } \Gamma_j \times \mathbb{R}^+ & \text{(21c)} \\ X(\cdot, 0) = 0 & \text{in } \Omega_j^c & \text{(21d)} \end{cases}$$

The ASM using such exact TBCs is optimal in the sense that it converges in two iterations, and no other ASM can converge faster [11].

We notice that in the ASM the IBCs for computing the solution in each subdomain are always written as function of the solution in the neighbor domains in the previous iteration, as in equation (20).

Let $E_j^k = (e_j^k, v_j^k)^T$ be the error of the DDM (compared to the monodomain solution) in subdomain Ω_j at iteration k, *i.e.*,

$$e_j^k = \eta|_{\Omega_j} - \eta_j^k, \qquad v_j^k = u|_{\Omega_j} - u_j^k$$

By linearity, such errors satisfy

$$\begin{cases} \mathcal{L}_{lin}\left(E_j^k\right) = 0 & \text{in } \Omega_j \times \mathbb{R}^+ \quad (22a) \\ E_j^k = 0 & \text{on } \partial\Omega_j \backslash \Gamma_j \times \mathbb{R}^+ \quad (22b) \\ \mathcal{B}_j(E_j^k) = \mathcal{B}(E_{j'}^{k-1}) & \text{on } \Gamma_j \times \mathbb{R}^+ \quad (22c) \\ E_j^k(\cdot, 0) = 0 & \text{in } \Omega_j \quad (22d) \end{cases}$$

Our goal is to assure, in (22c), that $\mathcal{B}(E_{j'}^{k-1}) = 0$, so (22a)-(22d) becomes an homogeneous system and therefore its solution E_j^k is zero, *i.e.*, $\mathcal{B}_j$ are perfectly TBCs (the problem (22a)-(22d) is assumed to be well-posed, and we work on the proof in Section 6 of this report).

We study the error in an infinite domain. Admitting that both subdomains are semi-infinite, under the form

$$\Omega_1 =]-\infty, L], \qquad \Omega_2 = [0, \infty[$$

with $L \geq 0$. System (22a)-(22d) is then written as

$$\begin{cases} \mathcal{L}_{lin}\left(E_j^k\right) = 0 & \text{in } \Omega_j \times \mathbb{R}^+ \quad (23a) \\ E_j^k \to 0 & |x| \to \infty \times \mathbb{R}^+ \quad (23b) \\ \mathcal{B}_j(E_j^k) = \mathcal{B}(E_{j'}^{k-1}) & \text{on } \Gamma_j \times \mathbb{R}^+ \quad (23c) \\ E_j^k(\cdot, 0) = 0 & \text{in } \Omega_j \quad (23d) \end{cases}$$

We perform a Laplace transform of (22b), with $\hat{f}$ denoting the Laplace transform of a function f and $s = \varepsilon + \xi i$, $\varepsilon, \xi \in \mathbb{R}$ denoting the Laplace frequency (with real part $\varepsilon > 0$, which physically means that f decays exponentially at rate ε [8]):

$$\begin{cases} s\hat{e}_j^k + h_0 \dfrac{\partial}{\partial x}\hat{v}_j^k + u_0 \dfrac{\partial}{\partial x}\hat{e}_j^k + \tilde{h}\dfrac{\partial^3}{\partial x^3}\hat{v}_j^k = 0 & \text{in } \Omega_j \quad (24a) \\ s\hat{v}_j^k - u_0 + u_0 \dfrac{\partial}{\partial x}\hat{v}_j^k + g\dfrac{\partial}{\partial x}\hat{e}_j^k + \overline{h}\dfrac{\partial^2}{\partial x^2}\left[s\hat{v}_j^k - u_0\right] = 0 & \text{in } \Omega_j \quad (24b) \\ \hat{E}_j^k \to 0 & |x| \to \infty \quad (24c) \\ \hat{\mathcal{B}}_j(\hat{E}_j^k) = \hat{\mathcal{B}}_j(\hat{E}_{j'}^{k-1}) & \text{on } \Gamma_j \quad (24d) \end{cases}$$

We seek a solution under the form

$$\hat{E}_j^k(s, x) = \begin{pmatrix} \overline{e}_j^k(s) \\ \overline{v}_j^k(s) \end{pmatrix} \exp\left(\lambda(s)x\right)$$

and we consider as an additional simplification that $u_0 = 0$.

Replacing in (24a)-(24b), we get the system

$$\begin{pmatrix} s & h_0\lambda + \tilde{h}\lambda^3 \\ g\lambda & s + \overline{h}\lambda^2 s \end{pmatrix} \begin{pmatrix} \overline{e}_j^k(s) \\ \overline{v}_j^k(s) \end{pmatrix} = 0$$

which admits nontrivial solutions iff the determinant of the matrix is zero, *i.e.*

$$g\tilde{h}\lambda^4 + (gh_0 - \overline{h}s^2)\lambda^2 - s^2 = 0 \tag{25}$$

The roots of (25) satisfy

$$Re(\lambda_1) > 0, \qquad Re(\lambda_2) < 0, \qquad Re(\lambda_3)\xi > 0, \qquad Re(\lambda_4)\xi < 0$$

which is proved in Appendix 1 of this report.

The solutions of (24a)-(24d) are then written under the form of the following linear combination:

$$\hat{E}_j^k = \sum_{l=1}^{4} \gamma_j^k \Phi_l \exp(\lambda_l x), \qquad j = 1, 2 \tag{26}$$

where $\mathbf{\Phi}_l$ is the eigenvector associated to the eigenvalue 0 and corresponding to λ_l. These eigenvectors can be written as

$$\mathbf{\Phi}_l = \begin{pmatrix} h_0\lambda_l + \tilde{h}\lambda_l^3 \\ -s \end{pmatrix}$$

In expression (26), we must decide, for $\hat{E}_1^k$ and $\hat{E}_2^k$ which coefficients among $\gamma_l^k,\ l = 1, ..., 4$, must be kept to zero, in order to force the exponentials to vanish at infinity (thus fulfilling the condition (24c)). For $\hat{E}_1^k$, defined in Ω_1, we keep the roots λ_l with positive real part; for $\hat{E}_2^k$, defined in Ω_2, we keep those with negative real part. Therefore, admitting that $\xi > 0$ (which assures to the Laplace transform a physical sense), we write

$$\hat{E}_1^k = \gamma_1^k \mathbf{\Phi}_1 \exp(\lambda_1 x) + \gamma_3^k \mathbf{\Phi}_3 \exp(\lambda_3 x)$$
$$\hat{E}_2^k = \gamma_2^k \mathbf{\Phi}_2 \exp(\lambda_2 x) + \gamma_4^k \mathbf{\Phi}_4 \exp(\lambda_4 x)$$

As said above, the operators S_j can be determined by imposing that the right side of the IBCs in (24d) are equal to 0. We explicit the computation of $\hat{S}_1$:

$$\hat{S}_1 \begin{pmatrix} \hat{e}_2^{k-1} \\ \hat{v}_2^{k-1} \end{pmatrix} = \begin{pmatrix} h_0\hat{v}_2^{k-1} + \tilde{h}\left(\hat{v}_2^{k-1}\right)_{xx} \\ g\hat{e}_2^{k-1} + \overline{h}\left(\hat{v}_2^{k-1}\right)_{xt} \end{pmatrix} =$$
$$= \begin{pmatrix} -s\left(h_0 + \tilde{h}\lambda_2^2\right)\gamma_2^{k-1}\exp(\lambda_2 x) - s\left(h_0 + \tilde{h}\lambda_4^2\right)\gamma_4^{k-1}\exp(\lambda_4 x) \\ \lambda_2\left(g\left(h_0 + \tilde{h}\lambda_2^2\right) - s^2\overline{h}\right)\gamma_2^{k-1}\exp(\lambda_2 x) + \lambda_4\left(g\left(h_0 + \tilde{h}\lambda_4^2\right) - s^2\overline{h}\right)\gamma_4^{k-1}\exp(\lambda_4 x) \end{pmatrix} \tag{27}$$

Writing $\hat{S}_j$ under the form

$$\hat{S}_j = \begin{pmatrix} \hat{S}_j^{\eta,\eta} & \hat{S}_j^{\eta,u} \\ \hat{S}_j^{u,\eta} & \hat{S}_j^{u,u} \end{pmatrix} \tag{28}$$

we have, matching the coefficients for each function $e^{\lambda_i x},\ i = 1, ..., 4,$, that the first and the second components of (27) leads respectively to the resolution of the linear systems :

$$M\begin{pmatrix} \hat{S}_1^{\eta,\eta} \\ \hat{S}_1^{\eta,u} \end{pmatrix} = \begin{pmatrix} -s\left(h_0+\tilde{h}\lambda_2^2\right) \\ -s\left(h_0+\tilde{h}\lambda_4^2\right) \end{pmatrix}$$

and

$$M\begin{pmatrix} \hat{S}_1^{u,\eta} \\ \hat{S}_1^{u,u} \end{pmatrix} = \begin{pmatrix} \lambda_2\left(g\left(h_0+\tilde{h}\lambda_2^2\right)-s^2\overline{h}\right) \\ \lambda_4\left(g\left(h_0+\tilde{h}\lambda_4^2\right)-s^2\overline{h}\right) \end{pmatrix} \tag{29}$$

with

$$M = \begin{pmatrix} h_0\lambda_2+\tilde{h}\lambda_2^3 & -s \\ h_0\lambda_4+\tilde{h}\lambda_4^3 & -s \end{pmatrix} \tag{30}$$

We obtain :

$$\hat{S}_1^{\eta,\eta} = \frac{-\tilde{h}s\left(\lambda_2+\lambda_4\right)}{h_0+\tilde{h}\left(\lambda_2^2+\lambda_2\lambda_4+\lambda_4^2\right)}, \qquad \hat{S}_1^{\eta,u} = \left(h_0+\tilde{h}\lambda_2^2\right)\left(1+\frac{\lambda_2}{s}\hat{S}_1^{\eta,\eta}\right)$$

$$\hat{S}_1^{u,\eta} = g - \frac{s^2\overline{h}}{h_0+\tilde{h}\left(\lambda_2^2+\lambda_2\lambda_4+\lambda_4^2\right)}, \qquad \hat{S}_1^{u,u} = s\overline{h}\lambda_2\left(1-\frac{h_0+\tilde{h}\lambda_2^2}{h_0+\tilde{h}\left(\lambda_2^2+\lambda_2\lambda_4+\lambda_4^2\right)}\right)$$

For writing these expressions under simpler forms, we consider, as described in Appendix 1, approximations for the roots λ_i around small values of ε and ξ and we keep only the terms up to order 1 w.r.t. to these coefficients :

$$\lambda_2 = -\frac{1}{h_0\sqrt{|\beta|}}, \qquad \lambda_4 = -\frac{\varepsilon}{\sqrt{gh_0}} - \frac{i\xi}{h_0\sqrt{|\beta|}}$$

We also make use of the notation (also introduced in the Appendix)

$$\tilde{h} = \beta h_0^3, \qquad \overline{h} = \theta h_0^2, \qquad \beta,\theta < 0$$

Therefore, we have

$$\hat{S}_1^{\eta,\eta} = \frac{-\beta h_0^3(\varepsilon+i\xi)\left(-\frac{1}{h_0\sqrt{|\beta|}}-\frac{\varepsilon}{\sqrt{gh_0}}-\frac{i\xi}{h_0\sqrt{|\beta|}}\right)}{h_0+\beta h_0^3\left(\frac{1}{h_0^2|\beta|}+\frac{\varepsilon+i\xi}{h_0^{3/2}\sqrt{g|\beta|}}\right)} = \sqrt{gh_0}$$

$$\hat{S}_1^{\eta,u} = 0, \qquad \text{since } h_0+\tilde{h}\lambda_2^2 = 0$$

$$\hat{S}_1^{u,\eta} = g - \frac{s^2\theta h_0^2}{-\frac{h_0^{3/2}}{\sqrt{g}}\sqrt{|\beta|}s} = g + s\frac{\theta}{\sqrt{|\beta|}}\sqrt{gh_0}$$

$$\hat{S}_1^{u,u} = s\overline{h}\lambda_2 = -sh_0\frac{\theta}{\sqrt{|\beta|}}$$

so, we obtain the approximate operator

$$\hat{S}_1^{app} = \begin{pmatrix} \sqrt{gh_0} & 0 \\ g+s\zeta\sqrt{gh_0} & -sh_0\zeta \end{pmatrix}$$

with $\zeta = \theta/\sqrt{|\beta|}$ fixed.

Similarly, we compute

$$\hat{S}_2^{app} = \begin{pmatrix} \sqrt{gh_0} & 0 \\ -g - s\zeta\sqrt{gh_0} & -sh_0\zeta \end{pmatrix}$$

Finally, an inverse Laplace Transform results in the followings approximate TBCs

$$\begin{aligned} \mathcal{B}_1^{app}(X) &= \begin{pmatrix} h_0 u + \tilde{h} u_{xx} - \sqrt{gh_0}\eta \\ \overline{h} u_{xt} - \zeta\sqrt{gh_0}\eta_t + h_0\zeta u_t \end{pmatrix} \\ \mathcal{B}_2^{app}(X) &= \begin{pmatrix} -h_0 u - \tilde{h} u_{xx} - \sqrt{gh_0}\eta \\ -\overline{h} u_{xt} + \zeta\sqrt{gh_0}\eta_t + h_0\zeta u_t \end{pmatrix} \end{aligned} \tag{31}$$

Therefore, we have constructed relatively simple operators, containing derivatives up to second order in space and first order in time. These operators can be used in the DDM problem (19a)-(19d), under the form (20). As these operators were obtained by performing several simplifications, we shall instead consider operators with generic coefficients to be optimized in terms of the numerical rate of convergence of the DDM (19a)-(19d) (with initial guesses suggested by the coefficients in operators (31)):

$$\begin{aligned} \tilde{\mathcal{B}}_1^{app}(X) &= \begin{pmatrix} a_1 u + a_2 u_{xx} - a_3\eta \\ a_4 u_{xt} - a_5\eta_t + a_6 u_t \end{pmatrix} \\ \tilde{\mathcal{B}}_2^{app}(X) &= \begin{pmatrix} -a_1 u - a_2 u_{xx} - a_3\eta \\ -a_4 u_{xt} + a_5\eta_t + a_6 u_t \end{pmatrix} \end{aligned} \tag{32}$$

The next steps in this work consist in implementing, testing and optimizing such conditions, initially for the simplified Boussinesq system (18a)-(18d), and then for the full governing equations (7) solved by BOSZ. We also have to show the well-posedness of the DDM (19a)-(19d) when using the operators (32) as IBCs.

6 Study of the well-posedness of the problem using the proposed TBCs

In this section, we seek to prove the well-posedness of the following system, corresponding to the linearized version of the equations solved by BOSZ:

$$\begin{cases} \eta_t + h_0 u_x + u_0 \eta_x + \tilde{h} u_{xxx} = 0 & \text{in } \Omega \quad (33a) \\ u_t + u_0 u_x + g\eta_x + \overline{h} u_{xxt} = 0 & \text{in } \Omega \quad (33b) \\ \text{TBC} & \text{on } \partial\Omega \quad (33c) \\ \boldsymbol{X}(\cdot, 0) = \boldsymbol{X}^{ini} & \text{in } \Omega \quad (33d) \end{cases}$$

where $\boldsymbol{X}(x,t) = (\eta(x,t), u(x,t))$ and $\tilde{h}, \hat{h} < 0$.

In order to simplificate this study, we perform the changing of variables

$$x \to x - u_0 t$$

For any function $f = f(x,t)$, we define

$$\tilde{f}(x,t) = f(x - u_0 t, t)$$

Then, dropping the tildes, the system (33a)-(33d) is rewritten as

$$\begin{cases} \eta_t + h_0 u_x + \tilde{h} u_{xxx} = 0 & \text{in } \Omega \quad (34a) \\ u_t + g\eta_x + \overline{h} u_{xxt} = 0 & \text{in } \Omega \quad (34b) \\ \text{TBC} & \text{on } \partial\Omega \quad (34c) \\ \boldsymbol{X}(\cdot, 0) = \boldsymbol{X}^{ini} & \text{in } \Omega \quad (34d) \end{cases}$$

Therefore, such changing of variables is equivalent to solve the system (33a)-(33d) considering $u_0 = 0$.

The boundary conditions, denoted as TBCs in (34c), are the approximate operators derived in the previous section. As, with the changing of variables, the equation (34a) for the evolution of η contains only time derivatives for η, only the equation (34b) requires boundary conditions.

The proof developed here follows the same approach as in [15, 7, 13], which consists on:

- Considering a given u, solve equation (34a) for η and write it under the form of an integral operator;
- Considering a given η, solve equation (34b) for u and write it under the form of an integral operator;
- Using a fixed-point theorem for proving the local existence (in time) of a solution;
- Using the Gronwall's lemma, prove the uniqueness of the solution.

Details on the inversion of the differential operators follows [9].

6.1 Derivation of an expression for η

In this case, the derivation is relativly simple. We solve the problem

$$\begin{cases} \eta_t = -h_0 u_x - \tilde{h} u_{xxx}, & x \in \Omega, t > 0 \\ \eta(x,0) = \eta^{ini}(x), & x \in \Omega \end{cases} \tag{35}$$

Integrating (35), we obtain

$$\eta(x,t) = \eta^{ini}(x) - \int_0^t \Big(h_0 u_x(x,s) + \tilde{h} u_{xxx}(x,s) \Big)\, ds \tag{36}$$

6.2 Derivation of an expression for u

We consider the equation (34b), corresponding to the evolution of u, with η as a given data. For simplicity, we consider a domain $\Omega = [0, L_0]$, and the following initial and boundary conditions, written from (31):

$$\alpha_{L,R} := \left(1 + \delta_{L,R} \frac{a_4}{a_6} \partial x\right) u_t|_{x=0,L_0} = \delta_{L,R} \frac{a_5}{a_6} \eta_t + \beta_{L,R} \tag{37}$$

$$u(x,0) = u^{ini}(x) \tag{38}$$

where

$$\delta_{L,R} = \begin{cases} \delta_L = -1, & x = 0 \\ \delta_R = 1, & x = L_0 \end{cases} \tag{39}$$

with L and R standing respectively for the left and the right boundaries. $\beta_{L,R}$ are given data, for example, the data from outside the domain:

$$\beta_{L,R} := \delta_{L,R} \frac{a_4}{a_6} (u^{out}_{L,R})_{xt} - \delta_{L,R} \frac{a_5}{a_6} (\eta^{out}_{L,R})_t + (u^{out}_{L,R})_t \tag{40}$$

We synthetize here the final result. See details of this derivation on Appendix 2. The solution u can be written as

$$\begin{aligned} u(x,t) =& u^{ini}(x) + \int_0^t \int_0^{L_0} K(x,y) g \eta dy ds \\ &+ \frac{N(L_0 - x)}{M(L_0)} \int_0^t \left[\alpha_L + \overline{\sigma}^2 \frac{a_4}{a_6} g \eta(0,s) \right] ds \\ &+ \frac{N(x)}{M(L_0)} \int_0^t \left[\alpha_R - \overline{\sigma}^2 \frac{a_4}{a_6} g \eta(L_0,s) \right] ds \end{aligned} \tag{41}$$

where

$$\begin{aligned} K(x,y) = \quad & \frac{\overline{\sigma}^2}{2} \Big[sign(x-y) e^{-\overline{\sigma}|x-y|} + \\ & - \frac{1}{M(L_0)} \left(1 - \overline{\sigma} \frac{a_4}{a_6}\right)^2 e^{-\overline{\sigma} L_0} \sinh(\overline{\sigma}(x-y)) \\ & + \frac{1}{M(L_0)} \left(1 - \left(\overline{\sigma} \frac{a_4}{a_6}\right)^2\right) \sinh(\overline{\sigma}(L_0 - x - y)) \Big] \end{aligned} \tag{42}$$

$$N(x) = \sinh(\overline{\sigma}x) + \overline{\sigma}\frac{a_4}{a_6}\cosh(\overline{\sigma}x) \tag{43}$$

$$M(x) = \left(1 + \left(\overline{\sigma}\frac{a_4}{a_6}\right)^2\right)\sinh(\overline{\sigma}x) + 2\overline{\sigma}\frac{a_4}{a_6}\cosh(\overline{\sigma}x) \tag{44}$$

From (37), we also write explicitly the integrals in time of the boundary conditions:

$$\int_0^t \alpha_L ds = -\frac{a_5}{a_6}\left[\eta(0,t) - \eta_0(0)\right] + \int_0^t \beta_L ds$$

$$\int_0^t \alpha_R ds = \frac{a_5}{a_6}\left[\eta(L_0,t) - \eta_0(L_0)\right] + \int_0^t \beta_R ds$$

As a conclusion, based on expressions (36) and (41), we write the system (34a)-(34d) under the form

$$\boldsymbol{X} = \boldsymbol{A}\boldsymbol{X}$$

with $\boldsymbol{A} := (A_\eta, A_u)^T$ and

$$A_\eta \boldsymbol{X} = \eta^{ini}(x) - \int_0^t \left(h_0 u_x(x,s) + \tilde{h} u_{xxx}(x,s)\right) ds$$

$$\begin{aligned} A_u \boldsymbol{X} =& u^{ini}(x) + \int_0^t \int_0^{L_0} K(x,y) g\eta dy ds \\ &+ \frac{N(L_0 - x)}{M(L_0)} \int_0^t \left[\alpha_L + \overline{\sigma}^2 \frac{a_4}{a_6} g\eta(0,s)\right] ds \\ &+ \frac{N(x)}{M(L_0)} \int_0^t \left[\alpha_R - \overline{\sigma}^2 \frac{a_4}{a_6} g\eta(L_0,s)\right] ds \end{aligned}$$

6.3 Spaces and norms

Before proving the existence and uniqueness of a solution, we define the Banach spaces and their respcetive norms to be considered here.

We denote by $C^k(a,b)$ the Banach space of the k-times continuously differentiable functions in $[a,b]$, equipped with the norm

$$\|f\|_{C^k(a,b)} = \sup_{0\le j\le k} \sup_{a\le x\le b} |f^{(j)}(x)|$$

In the case $k = 0$, we denote

$$||f|| = \sup_{a\le x\le b} |f(x)|$$

and

$$||\boldsymbol{f}|| = \max_{1\le i\le n} \|f_i(x)\|$$

for $\boldsymbol{f} = (f_1, ..., f_n) \in (C(a,b))^n$.

We also consider, for any Banach space X, the Banach space $C(0,T;X)$ of the continuous maps $u:[0,T]\to X$, equipped with the norm

$$||u||_{C(0,T;X)}=\sup_{0\leq t\leq T}||u(t)||_X$$

6.4 Estimations on the kernel K

We present in this subsections some estimations on the norm of the kernel K of the integral operator (41).

We define the operator

$$\mathcal{M}(v)(x)=\int_0^{L_0}K(x,y)v(y)dy$$

which satisfies the following property: if $v\in C^k(0,L_0)$, then $\mathcal{M}(v)\in C^{k+1}(0,L_0)$ and there is a constant $D_k=D_k(k,L_0)$ such that

$$\|\mathcal{M}(v)\|_{C^{k+1}(0,L_0)}\leq D_k\|v\|_{C^k}$$

Details on the derivation of D_k can be found in Appendix 3. We are specially interested here in

$$D_3=\max\{c_K+\overline{\sigma}^2,2\overline{\sigma}^2\max\{1,c_K\},2\overline{\sigma}^2\max\{1,2(c_K+\overline{\sigma}^2)\}\}$$

with

$$c_K=\frac{\overline{\sigma}^2}{2}L_0\left(1+\frac{\left(1-\overline{\sigma}\frac{a_4}{a_6}\right)^2+\left(\overline{\sigma}\frac{a_4}{a_6}\right)^2}{1+\left(\overline{\sigma}\frac{a_4}{a_6}\right)^2}\right)$$

6.5 Local existence of a solution

Let $\hat{C}(0,L_0):=\left\{v\in C(0,T_0;C^2(0,L_0)),\|v\|_{C^2(0,L_0)}\leq\|v\|\right\}$ and $\tilde{\mathcal{C}}:=C(0,T;\hat{C}(0,L_0))\times C(0,T;C^3(0,L_0))$.

We prove here that, for some $T,L_0>0$, $\boldsymbol{X}^{ini}\in\hat{C}(0,L_0)\times C^3(0,L_0)$ and $\beta_{L,R}\in C(0,T)\times C(0,T)$, there is a $T_0\leq T$ such that there is, for the problem (34a)-(34d), a solution $\boldsymbol{X}\in\tilde{\mathcal{C}}$.

The norm of $\tilde{\mathcal{C}}$ is defined as

$$\|\boldsymbol{v}\|_{\tilde{\mathcal{C}}}=\max\left\{\|v_1\|_{C(0,T;\hat{C}(0,L_0))},\|v_2\|_{C(0,T;C^3(0,L_0))}\right\}$$

Let $\boldsymbol{X}$ and $\tilde{\boldsymbol{X}}$ be two solutions in $\tilde{\mathcal{C}}\bigcap\mathcal{B}(0,r)$ (the ball of radius r centered in 0). Denoting $\phi(x):=\mathcal{M}(g(\eta-\tilde{\eta}))$, we have the following estimations

$$\begin{aligned}\left\|A_\eta\boldsymbol{X}-A_\eta\tilde{\boldsymbol{X}}\right\|_{C(0,T;\hat{C}(0,L_0))}&\leq\sup_{0\leq t\leq T_0}\sup_{0\leq x\leq L}\int_0^{T_0}\left|h_0\left(u_x-\tilde{u}_x\right)+\tilde{h}\left(u_{xxx}-\tilde{u}_{xxx}\right)\right|ds\\&\leq T_0\left(h_0\|u_x-\tilde{u}_x\|_{C(0,T_0;C(0,L))}+|\tilde{h}|\,\|u_{xxx}-\tilde{u}_{xxx}\|_{C(0,T_0;C(0,L))}\right)\\&\leq 2T_0\max\{h_0,|\tilde{h}|\}\,\|u-\tilde{u}\|_{C(0,T;C^3(0,L_0))}\end{aligned}$$

$$\begin{aligned}\left\|A_u\boldsymbol{X}-A_u\tilde{\boldsymbol{X}}\right\|_{C(0,T;C^3(0,L_0))} &= \sup_{0\le t\le T_0}\sup_{0\le j\le 3}\sup_{0\le x\le L}\int_0^{T_0}|\phi^{(j)}|(x)ds\\ &\le T_0\sup_{0\le t\le T_0}\|\phi\|_{C^3(0,L)} \le T_0D_3\sup_{0\le t\le T_0}\|g(\eta-\tilde{\eta})\|_{C^2(0,L)}\\ &\le T_0gD_3\left\|\eta-\tilde{\eta}\right\|_{C(0,T;\hat{C}(0,L_0))}\end{aligned}$$

Then,

$$\left\|\boldsymbol{A}\boldsymbol{X}-\boldsymbol{A}\tilde{\boldsymbol{X}}\right\|_{\tilde{\mathcal{C}}}\le\Theta\left\|\boldsymbol{X}-\tilde{\boldsymbol{X}}\right\|_{\tilde{\mathcal{C}}} \tag{45}$$

with

$$\Theta:=T_0\max\{gD_3,2\max\{h_0,|\tilde{h}|\}\} \tag{46}$$

For $\boldsymbol{X}\in\mathcal{B}(0,r)$, we denote $\boldsymbol{B}(x,t)=(B_\eta(x,t),B_u(x,t))$ the terms involving the initial and boundary conditions, with

$$B_\eta(x,t)=\eta^{ini}(x)$$

$$\begin{aligned}B_u(x,t)=&u^{ini}(x)\\ &+\frac{N(L_0-x)}{M(L_0)}\left[-\frac{a_5}{a_6}(\eta(0,t)-\eta^{ini}(0))+\int_0^t\left(\overline{\sigma}^2\frac{a_4}{a_6}g\eta(0,s)+\beta_L\right)ds\right]\\ &+\frac{N(x)}{M(L_0)}\left[\frac{a_5}{a_6}(\eta(L_0,t)-\eta^{ini}(L_0))-\int_0^t\left(\overline{\sigma}^2\frac{a_4}{a_6}g\eta(L_0,s)+\beta_R\right)ds\right]\end{aligned}$$

We have the following norm estimations:

$$\|B_\eta\|_{C(0,T;\hat{C}(0,L_0))}\le\sup_{0\le t\le T_0}\sup_{0\le x\le L_0}\left|\eta^{ini}\right|=\left\|\eta^{ini}\right\|_{C(0,L)}$$

$$\begin{aligned}\|B_u\|_{C(0,T;C^3(0,L_0))} &\le\left\|u^{ini}\right\|_{C^3(0,L_0)}\\ &+2\frac{1}{1+\left(\overline{\sigma}\frac{a_4}{a_6}\right)^2}\left(1+\overline{\sigma}\frac{a_4}{a_6}\frac{1+e^{-2L_0}}{1-e^{-2L_0}}\right)\left[\left|\frac{a_5}{a_6}\right|\left(\|\boldsymbol{\eta_b}\|_{C(0,L_0)}+\left\|\eta^{ini}\right\|_{C(0,L_0)}\right)\right.\\ &\left.+T_0\left(\overline{\sigma}^2\frac{a_4}{a_6}g\|\boldsymbol{\eta_b}\|_{C(0,L_0)}+\|\boldsymbol{\beta}\|_{C(0,T)}\right)\right]\end{aligned}$$

Then

$$\begin{aligned}\|\boldsymbol{B}\|_{\tilde{\mathcal{C}}}\le b:=&\left(1+\psi\left|\frac{a_5}{a_6}\right|\right)\left\|\boldsymbol{X}^{ini}\right\|_{\hat{C}(0,L_0)\times C^3(0,L_0)}\\ &+\psi\left(\left|\frac{a_5}{a_6}\right|+T_0\overline{\sigma}^2\frac{a_4}{a_6}g\right)\|\boldsymbol{\eta_b}\|_{C(0,T)}+\psi T_0\|\boldsymbol{\beta}\|_{C(0,T)}\end{aligned} \tag{47}$$

with

$$\psi = 2\frac{1}{1+\left(\overline{\sigma}\frac{a_4}{a_6}\right)^2}\left(1+\overline{\sigma}\frac{a_4}{a_6}\frac{1+e^{-2L_0}}{1-e^{-2L_0}}\right)$$

Then

$$\|\boldsymbol{AX}\|_{\tilde{\mathcal{C}}} = \|\boldsymbol{AX} - \boldsymbol{A0} + B\|_{\tilde{\mathcal{C}}} \leq \Theta r + b$$

Taking

$$r = 2b, \qquad \Theta = \frac{1}{2} \tag{48}$$

we have

$$\|\boldsymbol{AX}\|_{\tilde{\mathcal{C}}} \leq r$$

This last result means that $\boldsymbol{A}$ is a contracting mapping from $\tilde{\mathcal{C}} \bigcap \mathcal{B}(0,r)$ into $\tilde{\mathcal{C}} \bigcap \mathcal{B}(0,r)$. Using the contraction-mapping (or fixed point) theorem, we can state the local existence (within $0 \leq t \leq T_0$) of a solution for (33a)-(33d).

Let us notice that there is a $T_0 > 0$ such that $\Theta = 1/2$, which can be easily seen in expression (46).

Nevertheless, it is necessary to remark some unsolved issues on the proof developed above. Firstly, as we can see in equation (47), the norm estimation for $\boldsymbol{B}$ depends on the boundary values of η, for which we do not have any a priori estimation (we recall that, in the system (34a)-(34b), it is not required boundary conditions for η).

Secondly, for imposing that both $\boldsymbol{X}$ and $\boldsymbol{AX}$ are in the same space, we had to define a quite unusual space for η, requiring that it is continuously differentiably up to the second derivative, but with its norm majorated by η itself.

Finally, as with the changing of variables performed we get rid of the boundary conditions for η, the norm majorations do not depend explictly on the coefficients a_1, a_2 and a_3 of our TBCs.

6.6 Uniqueness of the solution

If $\boldsymbol{X}$ and $\tilde{\boldsymbol{X}}$ are two solutions of (33a)-(33d) in $\tilde{\mathcal{C}}$, and $\hat{\boldsymbol{X}} = \boldsymbol{X} - \tilde{\boldsymbol{X}}$, we show, in a similar way as above, that

$$\left\|\hat{\boldsymbol{X}}\right\|_{\tilde{\mathcal{C}}} = \left\|\boldsymbol{A}\hat{\boldsymbol{X}}\right\|_{\tilde{\mathcal{C}}} \leq c\int_0^t \left\|\hat{\boldsymbol{X}}\right\|_{\tilde{\mathcal{C}}} ds = \lambda + c\int_0^t \left\|\hat{\boldsymbol{X}}\right\|_{\tilde{\mathcal{C}}} ds$$

with $0 \leq t \leq T_1$ and $\lambda = 0$. The Gronwall's lemma implies that

$$\left\|\hat{\boldsymbol{X}}\right\|_{\tilde{\mathcal{C}}} \leq \lambda \exp\left(c\int_0^t ds\right) = 0$$

thus $\left\|\hat{\boldsymbol{X}}\right\|_{\tilde{\mathcal{C}}} = 0$ and $\hat{\boldsymbol{X}} = \boldsymbol{0}$.

7 Conclusion

In this report, we presented the achievements and results of the work developed in this project in MERIC. We constructed the basis for the proposed coupling scheme between a spectral model (WaveWatch III) and a Boussinesq-type model (BOSZ), and we proposed and studied trasnaprent boudnary conditions for the BOSZ model in order to improve the coupling. Both topics will permit to seek for further objectives in the sequel of this research.

In the first half of the project, the main work consisted fundamentally in structuring the coupling, from the point of view both of the implementation and the treating of different types of wave propagation models.

The coupling software OpenPALM, used for coupling the models, allows to synchronize their executions and run them in parallel. Facing various issues that prevented us from incorporating the models into PALM in a "traditional" way, we proposed an alternative approach that, even not optimal in terms of computational time, avoided the modification of the models' source codes and easily allows to configure the coupling for new test cases. Moreover, possible future modifications of the coupling scheme, including the use of other Boussinesq-type models or configuring 2D testcases, would be relatively straightforward.

For exchanging data between the models, we had to considerate the different types of variables used by them. While WW3, as a spectral model, solves a governing equation for the wave energy spectrum, *i.e.*, in the frequency domain, BOSZ, as a time-domain model, solves for the surface elevation and the velocity as function of time. Therefore, conversion procedures are required: we implemented the Welch's method for passing from the surface elevation timeseries to the energy spectrum; in the other way, a source function method (already implemented in BOSZ) is used. While the first case has been validated, the second one still remains relatively unclear, reducing the user control for imposing boundary conditions in BOSZ.

For testing the coupling scheme, we performed simulations in a testcase over a sandbank, and we compared the results with the simulations done with each individual model over the entire domain. We remark that this test case cannot be used for physical validation, as the reference output does not come from real data, but from a 2D WW3 simulation. Moreover, as each model has different properties and domains of validity, we cannot predict a "correct" result. Evidently, the WW3 simulations gave the results that are closest from the reference. Concerning the BOSZ model, we were able to evaluate its performance and energy damping with two alternatives for the discretization of the fluxes: a finite volume and a finite difference schemes; this last one showed to be much less dissipative, and then was chosen for the implementation.

The work deveoped in the second half of the project was motivated by our objective of implementing domain decomposition techniques in order to improve the coupling. In the first scheme proposed here, the informations were simply transmitted from one model to the other, always from offshore to the coast. The two last section of this report presents initial steps in this direction, where we study and propose approximate transparent boundary conditions for a linearized and simplified version of the equations solved by BOSZ.

The derivation of such operators was done following a classical approach for constructing approximate TBCs for linear equations. Such approach intend to ontour the difficults of obtaining and computing the exact TBCs. Then,

we obtained relatively simple operators, which are local in time, depending on a set of six coefficients that should be numerically optimized, concerning the numerical rate of convergence of a DDM problem using these operators as interface boundary conditions.

Nevertheless, before implementing these operators, it was necessary to prove that they lead to a well-posed problem. Even if we were able to advance on this proof, there are still unsolved issues concerning the proof of the local existence in time. Firstly, we had to impose the solution to be in an unusual space (limiting the application of the operators), and, secondly, the norm majorations depend on the boundary values of the surface elevation, for which we do not dispose of a priori estimations.

Therefore, among the following steps in the remaining months of the project, the first one will be the revision of this proof or the derivation of another approximate TBCs by an alternative approach, following other works in the litterature. If we succeed in this task, we will be able to implement, test and optimize the proposed operators. Evidently, for physically evaluating their results, we will need to consider a test case with real reference output data.

The implementation of these operators would be done in the following sequence: firstly, as boundary conditions for the linearized equations used to derive them; then, as IBCs for solving this equations with a DDM. After that, we would implement them in the full BOSZ equations (*i.e.*, the non linearized equations), expecting the operators to have a similar behaviour. Finally, after validating this step, we would return to the first half of the project and implement the operators in the coupling with WW3.

References

[1] Antoine, X., Arnold, A., Besse, C., Ehrhardt, M., and Schädle, C. A review of Transparent Boundary Conditions or linear and nonlinear Schrödinger equations. *Commum. Comput. Phys. 4*, 4 (October 2008), 729–796.

[2] Ardhuin, F., and Filipot, J.-F. Ocean waves in geosciences. Available in https://www.researchgate.net/publication/304990310_Ocean_Waves_in_Geosciences, October 2017.

[3] Bennis, A.-C., Ardhuin, F., and Odaka, T. Modélisation couplée vagues-courant : dévéloppements avec MARS3D et WAVEWATCH III. In *XIème Journées Nationales Génie Côtier - Génie Civil* (Les Sables d'Olonne, Juin 2010), Éditions Paralia CFL.

[4] Besse, C., Ehrhardt, M., and Lacroix-Violet, I. Discrete Artificial Boundary Conditions for the linearized Korteweg-de Vries Equation. *Numer. Meth. Part. D. E. 32*, 5 (Sept. 2016), 1455–1484.

[5] Blayo, E., Cherel, D., and Rousseau, A. Towards optimized schwarz methods for the navier–stokes equations. *J. Sci. Computing 66*, 1 (Jan 2016), 275–295.

[6] Blayo, E., Rousseau, A., and Tayachi, M. Boundary conditions and Schwarz waveform relaxation method for linear viscous Shallow Water equations in hydrodynamics. *SMAI Journal of Computational Mathematics 3* (2017), 117–137.

[7] Bona, J. L., and Chen, M. A boussinesq system for two-way propagation of nonlinear dispersive waves. *Physica D: Nonlinear Phenomena 116*, 1 (1998), 191 – 224.

[8] Chau, P. C. Laplace and Fourier transforms (Supplementary notes - Process Control (UCSD)). Available in http://www.cambridge.org/us/features/chau/webnotes/chap2laplace.pdf, 2000.

[9] Gregg, J. Lecture notes: Inverting a Differential Operator. Course of Partial Differential Equations in Lawrence University. Available in http://www2.lawrence.edu/fast/GREGGJ/Math400/Sections_9_1_and_9_2.pdf.

[10] Holthuijsen, L. H. *Waves in oceanic anc coastal waters*. Cambridge University Press, New York, 2007.

[11] Japhet, C., and Nataf, F. The best interface conditions for Domain Decompostion methods : Absorbing Boundary Conditions. https://www.ljll.math.upmc.fr/∼nataf/chapitre.pdf, January 2003.

[12] Nwogu, O. An alternative form of the Boussinesq equations for nearshore wave propagation. *J. Waterw. Port. Coast 119*, 6 (1993).

[13] Quintero, J. R., and Munoz, J. Existence and uniqueness for a boussinesq system with a disordered forcing. *Methods Appl. Anal. 11*, 1 (03 2004), 015–032.

[14] Roeber, V., and Cheung, K. F. Boussinesq-type model for energetic breaking waves in fringing reef environments. *Coast. Eng.*, 70 (2012), 1–20.

[15] Schonbek, M. E. Existence of solutions for the boussinesq system of equations. *Journal of Differential Equations 42*, 3 (1981), 325 – 352.

[16] The WAVEWATCH III®Development Group (WW3DG), 2016. *User manual and System Documentation of WAVEWATCH III®version 5.16*. Tech. Note 329, NOAA/NWS/NCEP/MMAB, College Park, MD, USA, 326 pp. + Appendices.

[17] Volker, R., Cheung, K. F., and Kobayashi, M. H. Shock-capturing boussinesq-type model for nearshore wave processes. *Coast. Eng. 57*, 4 (2010), 407 – 423.

[18] Wei, G., and Kirby, James T. andd Sinha, A. Generation of waves in Boussinesq models using a source function method. *Coast. Eng. 36* (1999), 271–299.

Appendix 1: study on the roots of the characteristic polynomial

Sign analysis

We are interested in studying the sign of the real part of the four roots $\lambda_l,\ l = 1, ..., 4$, of the characteristic polynomial (25), to decide which should be kept to zero such that condition (23b) is satisfied.

We follow the approach adopted by [4] for studying the TBCs for the Airy's equation. We write explicitly the real and the imaginary parts (respectively ε and ξ) of the frequency s and we perform a series expansion around $\varepsilon = 0$. We obtain

$$\begin{aligned} \lambda_1 &= A + iB\varepsilon + \mathcal{O}(\varepsilon^2), \qquad \lambda_2 = -\lambda_1 \\ \lambda_3 &= A' - iB'\varepsilon + \mathcal{O}(\varepsilon^2), \qquad \lambda_4 = -\lambda_3 \end{aligned}$$

with

$$\begin{aligned} A &= \sqrt{3}|\xi|\sqrt{-\frac{a+b+\sqrt{(a+b)^2-4(c+ab)}}{c+ab}} \\ B &= \frac{A}{2\xi}\frac{a-b-\sqrt{(a+b)^2-4(c+ab)}}{\sqrt{(a+b)^2-4(c+ab)}} \\ A' &= \sqrt{3}|\xi|\sqrt{\frac{-a-b+\sqrt{(a+b)^2-4(c+ab)}}{c+ab}} \\ B' &= \frac{A'}{2\xi}\frac{a-b+\sqrt{(a+b)^2-4(c+ab)}}{\sqrt{(a+b)^2-4(c+ab)}} \\ a = 6gh_0, \qquad b &= 3z(2h_0+z)\xi^2 = 3\alpha h_0^2(2+\alpha)\xi^2, \qquad c = 12gh_0^3\xi^2 \end{aligned}$$

For the definition of b, we wrote $z = \alpha h_0$, with $\alpha < 0$. In fact, as mentioned before, z is a reference depth in which the velocity is computed; as specified in [17], BOSZ uses the value $\alpha = -0.53753$, for which the model gives good results for depths in the range $0 < h/L_0 < 0.6$, where L_0 is the deep water wavelength.

Using this notation, we also rewrite the quantities $\tilde{h}$ and $\overline{h}$, which will be used later :

$$\begin{aligned} \tilde{h} &= \beta h_0^3, \qquad \beta = \frac{\alpha^2}{2} + \alpha + \frac{1}{3} \approx -0.06 < 0 \\ \overline{h} &= \theta h_0^2, \qquad \theta = \alpha\left(\frac{\alpha}{2}+1\right) \approx -0.4 < 0 \end{aligned} \tag{49}$$

The roots λ_i are function of h_0, ε and ξ. For studying the sign of their real part, we perform a preliminary investigation by plotting $Re(\lambda_i)$ in function of (h_0, ξ) for some fixed values of $\varepsilon > 0$. We intent to find some pattern in the sign of $Re(\lambda_i)$ that would motivate us to study its sign analytically. Figure 27 presents the results for $\varepsilon = 0.1$. Similar results were obtained for other values of $\varepsilon > 0$.

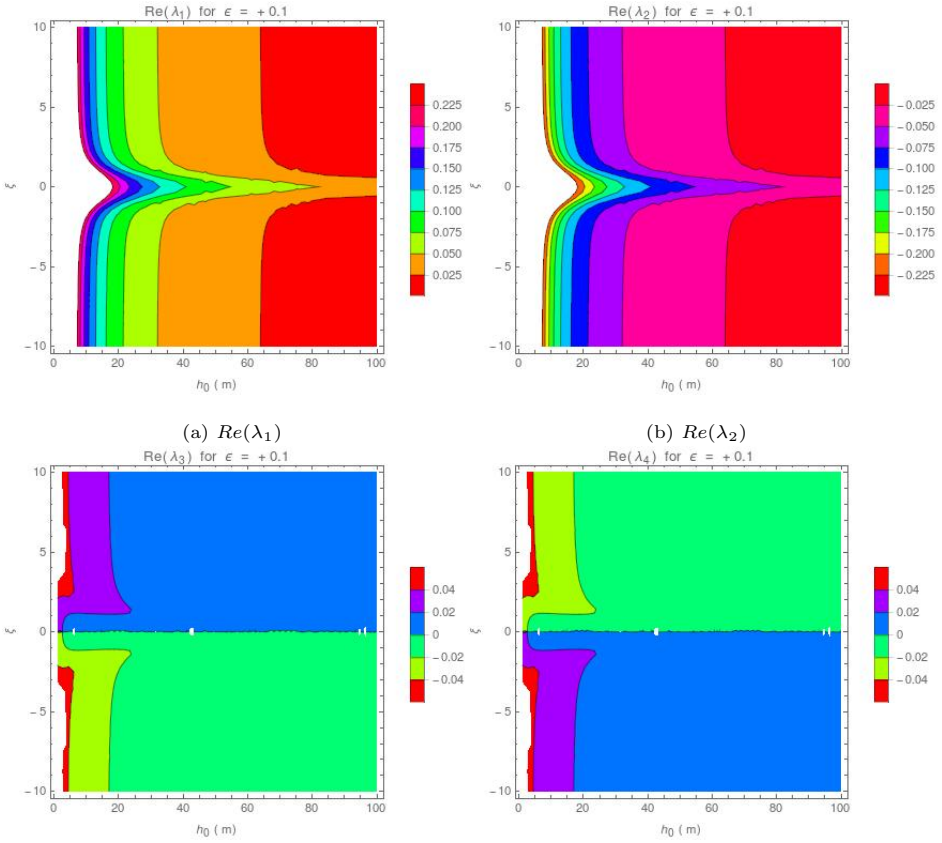

(a) $Re(\lambda_1)$ (b) $Re(\lambda_2)$

(c) $Re(\lambda_3)$ (d) $Re(\lambda_4)$

Figure 27: Real part of the roots λ_i in function of (h_0, ξ) for $\varepsilon = 0.1$

We can observe the sign of $Re(\lambda_1)$ and $Re(\lambda_2)$ are constant, and that the sign of $Re(\lambda_3)$ and $Re(\lambda_4)$ depends on the sign of ξ. Therefore, we study their signs analytically :

Study of $Re(\lambda_1)$ and $Re(\lambda_2)$

- In the definition of A, the denominator inside the square root is negative :
$$c + ab = 6gh_0^3\xi^2(2 + 3\alpha(2 + \alpha)) \approx -0.36gh_0^3\xi^2 < 0$$
- Thus, $(a+b)^2 - 4(c+ab) > (a+b)^2$ and $\sqrt{(a+b)^2 - 4(c+ab)} > |a+b|$; so the numerator of A is positive :
$$a + b + \sqrt{(a+b)^2 - 4(c+ab)} > a + b + |a+b| \geq 0$$
- As a conclusion
$$-\frac{a + b + \sqrt{(a+b)^2 - 4(c+ab)}}{c+ab} > 0 \tag{50}$$
so $A \in \mathbb{R}$.

- We also conclude that $B \in \mathbb{R}$. Therefore

$$\begin{aligned} Re(\lambda_1) = Re(A + iB\varepsilon) = A > 0, \\ Re(\lambda_2) = -A < 0 \end{aligned} \tag{51}$$

Study of $Re(\lambda_3)$ and $Re(\lambda_4)$

In a very similar reasoning:

- in the definition of A', the numerator is positive:

$$-a - b + \sqrt{(a+b)^2 - 4(c+ab)} > -(a+b) + |a+b| \geq 0 \tag{52}$$

  As the denominator is negative, we conclude that $A' \notin \mathbb{R}$ and $B' \notin \mathbb{R}$

- For studying the sign of B', we show that

$$a-b+\sqrt{(a+b)^2 - 4(c+ab)} > a-b+|a+b| = \begin{cases} 2a > 0, & \text{if } a+b > 0 \\ -2b > 0, & \text{else} \end{cases} \tag{53}$$

  And we write $B' = \sigma i |A'|/\xi$, with $\sigma > 0$.

- Finally,

$$Re(\lambda_3) = Re(A' - iB'\varepsilon) = \sigma |A'| \varepsilon / \xi, \tag{54}$$

  so

$$\begin{aligned} sgn(Re(\lambda_3)) = sgn(\xi) \\ sgn(Re(\lambda_4)) = -sgn(\xi) \end{aligned} \tag{55}$$

These conclusions are coherent with the results presented in Figure 27.

Further approximations

While approximations around small values of ε were enough for studying the sign of the roots λ_i of the characteristic polynomial (25), we need to consider further approximations for deriving simpler forms for the operators (28): we perform a series expansion of A, A', B, B' around $\xi = 0$ (which could be physically justified by the fact that ordinary wind waves have most of its energy spectrum concentrated around frequencies in the order of $10^{-1} Hz$ [10, 2]):

$$\begin{aligned} A = \frac{1}{h_0\sqrt{|\beta|}} + \mathcal{O}(\xi^2), \qquad A' = \frac{i\xi}{h_0\sqrt{|\beta|}} + \mathcal{O}(\xi^3), \\ B = \frac{\xi}{3g\sqrt{|\beta|}} + \mathcal{O}(\xi^3), \qquad B' = \frac{i}{\sqrt{gh_0}} + \mathcal{O}(\xi^2) \end{aligned} \tag{56}$$

with β defined in (49). Thus,

$$\begin{aligned} \lambda_1 = A + iB\varepsilon + \mathcal{O}(\varepsilon^2) = \frac{1}{h_0\sqrt{|\beta|}} + \mathcal{O}(\varepsilon^2, \xi^2, \varepsilon\xi), \qquad \lambda_2 = -\lambda_1 \\ \lambda_3 = A' - iB'\varepsilon + \mathcal{O}(\varepsilon^2) = \frac{\varepsilon}{\sqrt{gh_0}} + \frac{i\xi}{h_0\sqrt{|\beta|}} + \mathcal{O}(\varepsilon^2, \xi^2), \qquad \lambda_4 = -\lambda_3 \end{aligned} \tag{57}$$

Appendix 2: details on the derivation of an integral expression for $u(x,t)$

We present here the details of the derivation of the expression (41). We rewrite (34b) under the form

$$(1+\overline{h}\partial_{xx})u_t = -g\eta_x =: F(x) \tag{58}$$

We firstly search the solution $u_t = u_t(x)$ for (58), using the method of variation of parameters.

The homogeneous equation

$$(1+\overline{h}\partial_{xx})u_t = 0 \tag{59}$$

has the solutions

$$v_1(x) = e^{\overline{\sigma}x}, \qquad v_2(x) = e^{-\overline{\sigma}x}$$

where, recalling that $\overline{h} < 0$,

$$\overline{\sigma} = \frac{1}{\sqrt{|\overline{h}|}}$$

We will thus seek a solution for (58) under the form

$$u_t(x) = c_1(x)v_1(x) + c_2(x)v_2(x) \tag{60}$$

Taking the second derivative of (60) and supposing that

$$v_1(x)\frac{dc_1}{dx} + v_2(x)\frac{dc_2}{dx} = 0 \tag{61}$$

we get

$$\frac{d^2}{dx^2}u_t(x) = \frac{dc_1}{dx}\frac{dv_1}{dx} + \frac{dc_2}{dx}\frac{dv_2}{dx} + c_1(x)\frac{d^2v_1}{dx^2} + c_2(x)\frac{d^2v_2}{dx^2} \tag{62}$$

Replacing (62) into (58) and using the fact that v_1 and v_2 solve (59), we have

$$\frac{dc_1}{dx}\frac{dv_1}{dx} + \frac{dc_2}{dx}\frac{dv_2}{dx} = \frac{F(x)}{\overline{h}} \tag{63}$$

Equations (61) and (63) constitute a system on $(dc_1/dx, dc_2/dx)^T$, whose solution is

$$\begin{pmatrix} \frac{dc_1}{dx} \\ \frac{dc_2}{dx} \end{pmatrix} = \begin{pmatrix} -\frac{\overline{\sigma}}{2}v_2(x)F(x) \\ \frac{\overline{\sigma}}{2}v_1(x)F(x) \end{pmatrix}$$

Thus,

$$c_1(x) = \frac{\overline{\sigma}}{2}\int_x^L e^{-\overline{\sigma}y}F(y)dy + b_1, \qquad c_2(x) = \frac{\overline{\sigma}}{2}\int_0^x e^{\overline{\sigma}y}F(y)dy + b_2$$

which verifies the hypothesis (61). The constants b_1 and b_2 will be determined using the boundary conditions. For this, we replace the (60) into (37):

$$\alpha_{L,R} = c_1(x)v_1(x)\left(1 + \delta_{L,R}\overline{\sigma}\frac{a_4}{a_6}\right) + c_2(x)v_2(x)\left(1 - \delta_{L,R}\overline{\sigma}\frac{a_4}{a_6}\right)$$

Thus,

$$\alpha_L = \left[\frac{\overline{\sigma}}{2}\int_0^L e^{-\overline{\sigma}y}F(y)dy + b_1\right]\omega_L^+ + b_2\omega_L^- \tag{64}$$

$$\alpha_R = b_1 e^{\overline{\sigma}L}\omega_R^+ + \left[\frac{\overline{\sigma}}{2}\int_0^L e^{\overline{\sigma}y}F(y)dy + b_2\right]e^{-\overline{\sigma}L}\omega_R^- \tag{65}$$

where

$$\omega_{L,R}^{+,-} = 1 \pm \delta_{L,R}\overline{\sigma}\frac{a_4}{a_6}$$

Solving (64) and (65) for b_1 and b_2, we get

$$b_1 = \frac{\alpha_L}{\omega_L^+} + \frac{\omega_L^-}{\omega_R^-\omega_L^+ e^{-\overline{\sigma}L} - \omega_L^-\omega_R^+ e^{\overline{\sigma}L}}\left[\alpha_L\frac{\omega_R^+}{\omega_L^+}e^{\overline{\sigma}L} - \alpha_R\omega_L^- + \frac{\overline{\sigma}}{2}e^{-\overline{\sigma}L}\int_0^L 2N(y)F(y)dy\right]$$

$$b_2 = \frac{\omega_L^+}{\omega_R^-\omega_L^+ e^{-\overline{\sigma}L} - \omega_L^-\omega_R^+ e^{\overline{\sigma}L}}\left[\alpha_R - \alpha_L\frac{\omega_R^+}{\omega_L^-}e^{\overline{\sigma}L} + \frac{\overline{\sigma}}{2}\int_0^L 2N(L-y)F(y)dy\right]$$

where N is defined in (43).

Coming back to (60) and using the values of δ_L and δ_R as defined in (39), we obtain

$$u_t(x) = \int_0^L G(x,y)F(y)dy + \frac{N(L-x)}{M(L)}\alpha_L + \frac{N(x)}{M(L)}\alpha_R \tag{66}$$

where M is defined in (43) and

$$\begin{aligned} G(x,y) = \frac{\overline{\sigma}}{2}\Big[&e^{-\overline{\sigma}|x-y|} + \\ &+ \frac{1}{M(L)}\left(1 - \overline{\sigma}\frac{a_4}{a_6}\right)^2 e^{-\overline{\sigma}L}\cosh(\overline{\sigma}(x-y)) \\ &- \frac{1}{M(L)}\left(1 - \left(\overline{\sigma}\frac{a_4}{a_6}\right)^2\right)\cosh(\overline{\sigma}(L-x-y))\Big] \end{aligned}$$

We notice that, for all $x \in \Omega$,

$$G(x,0) = \overline{\sigma}^2\frac{a_4}{a_6}\frac{N(L-x)}{M(L)}, \qquad G(x,L) = \overline{\sigma}^2\frac{a_4}{a_6}\frac{N(x)}{M(L)}$$

Thus, recalling the definition of F and integrating (66) by parts w.r.t, and also integrating it in time, we finally get

$$
\begin{aligned}
u(x,t) =& u^{ini}(x) + \int_0^t \int_0^L K(x,y) g\eta dy ds \\
&+ \frac{N(L-x)}{M(L)} \int_0^t \left[\alpha_L + \overline{\sigma}^2 \frac{a_4}{a_6} g\eta(0,s) \right] ds \\
&+ \frac{N(x)}{M(L)} \int_0^t \left[\alpha_R - \overline{\sigma}^2 \frac{a_4}{a_6} g\eta(L,s) \right] ds
\end{aligned} \tag{67}
$$

with $K(x,y) := \partial G / \partial y(x,y)$ defined in (42)

Appendix 3: details on the norm estimations for the kernel K

Proof We have the following estimation on the norm of $\mathcal{M}(v),\ \forall v \in C(0,L)$:

$$\begin{aligned} ||\mathcal{M}(v)|| &= \sup_{0\le x\le L} |\int_0^L K(x,y)v(y)dy| \le \sup_{0\le x\le L} \int_0^L |K(x,y)v(y)|dy \\ &\le ||v|| \sup_{0\le x\le L} \int_0^L |K(x,y)|dy \\ &\le c_K||v|| \end{aligned} \tag{68}$$

with

$$c_K = \frac{\overline{\sigma}^2}{2} L \left(1 + \frac{\left(1-\overline{\sigma}\frac{a_4}{a_6}\right)^2 + \left(\overline{\sigma}\frac{a_4}{a_6}\right)^2}{1+\left(\overline{\sigma}\frac{a_4}{a_6}\right)^2} \right)$$

since, **supposing that** $a_4/a_6 > 0$,

$$\begin{aligned} \frac{\sinh(x)}{M(L)} &= \frac{\sinh(x)}{\left(1+\left(\overline{\sigma}\frac{a_4}{a_6}\right)^2\right)\sinh(x) + 2\overline{\sigma}\frac{a_4}{a_6}\cosh(x)} \\ &\le \frac{\sinh(x)}{\left(1+\left(\overline{\sigma}\frac{a_4}{a_6}\right)^2\right)\sinh(x)} \le \frac{1}{1+\left(\overline{\sigma}\frac{a_4}{a_6}\right)^2} \end{aligned} \tag{69}$$

and

$$\begin{aligned} \frac{\cosh(x)}{M(L)} &= \frac{\cosh(x)}{\left(1+\left(\overline{\sigma}\frac{a_4}{a_6}\right)^2\right)\sinh(L) + 2\overline{\sigma}\frac{a_4}{a_6}\cosh(L)} \\ &\le \frac{\cosh(x)}{\left(1+\left(\overline{\sigma}\frac{a_4}{a_6}\right)^2\right)\sinh(L)} \le \frac{1}{1+\left(\overline{\sigma}\frac{a_4}{a_6}\right)^2}\frac{1+e^{-2L}}{1-e^{-2L}} \end{aligned}$$

for every x such that $|x| < L$, thus

$$\begin{aligned} |K(x,y)| &\le \frac{\overline{\sigma}^2}{2}\left[1 + \frac{\left|\left(1-\overline{\sigma}\frac{a_4}{a_6}\right)^2\right|}{1+\left(\overline{\sigma}\frac{a_4}{a_6}\right)^2} + \frac{\left|1-\left(\overline{\sigma}\frac{a_4}{a_6}\right)^2\right|}{1+\left(\overline{\sigma}\frac{a_4}{a_6}\right)^2}\right] \\ &\le \frac{\overline{\sigma}^2}{2}\left(1 + \frac{\left(1-\overline{\sigma}\frac{a_4}{a_6}\right)^2 + \left(\overline{\sigma}\frac{a_4}{a_6}\right)^2}{1+\left(\overline{\sigma}\frac{a_4}{a_6}\right)^2}\right) \end{aligned} \tag{70}$$

We notice that, for each $x \in [0,L]$, $K(x,y)$ is continuous, except in $y = x$, where the jump of the function is

$$K(x,x^+) - K(x,x^-) = \overline{\sigma}^2$$

Then, denoting $\phi(x) = \mathcal{M}(v)$, we have

$$\phi'(x) = \int_0^L \frac{\partial}{\partial x} K(x,y) v(y) dy + \overline{\sigma}^2 v(x) \tag{71}$$

Noticing that, $\forall x \neq y$ and $\forall j \geq 0$

$$\frac{\partial^{j+2}}{\partial x^{j+2}} K(x,y) = \overline{\sigma}^2 \frac{\partial^j}{\partial x^j} K(x,y)$$

we have, for $j \leq 1$

$$\phi^{(j+2)}(x) = \overline{\sigma}^2 \phi^{(j)}(x) + \overline{\sigma}^2 v^{(j+1)}(x) \tag{72}$$

From (68) and (71), we have

$$\|\phi\|_{C^1(0,L)} = \max\{c_K, c_K + \overline{\sigma}^2\} \|v\| = (c_K + \overline{\sigma}^2) \|v\|$$

And, from the recurrence relation (72), one can obtain estimations on D_k. We compute here D_3:

$$\begin{aligned}
\left\|\phi^{(2)}\right\| &\leq \overline{\sigma}^2 \|\phi\| + \overline{\sigma}^2 \|v'\| \leq \overline{\sigma}^2 c_K \|v\| + \overline{\sigma}^2 \|v'\| \\
&\leq 2\overline{\sigma}^2 \max\{1, c_K\} \|v\|_{C^1(0,L)} \\
\left\|\phi^{(3)}\right\| &\leq \overline{\sigma}^2 \|\phi'\| + \leq^2 \|v''\| \leq 2\overline{\sigma}^2 (c_K + \overline{\sigma}^2) \|v\| + \overline{\sigma}^2 \|v''\| \\
&\leq 2\overline{\sigma}^2 \max\{1, 2(c_K + \overline{\sigma}^2)\} \|v\|_{C^2(0,L)}
\end{aligned}$$

Finally,

$$\|\phi\|_{C^3(0,L)} \leq D_3 \|v\|_{C^2(0,L)}$$

with

$$D_3 = \max\{c_K + \overline{\sigma}^2, 2\overline{\sigma}^2 \max\{1, c_K\}, 2\overline{\sigma}^2 \max\{1, 2(c_K + \overline{\sigma}^2)\}\}$$